AFRL-AFOSR-VA-TR-2019-0315

State-of-the-Art High-Flux Mono-Energetic Ion Sources Driven by Ultra-Intense Laser Pulses

Farhat Beg
UNIVERSITY OF CALIFORNIA, SAN DIEGO

03/06/2019
Final Report

Air Force Research Laboratory
AF Office Of Scientific Research (AFOSR)/ RTB1
Arlington, Virginia 22203
Air Force Materiel Command

REPORT DOCUMENTATION PAGE

Form Approved
OMB No. 0704-0188

1. REPORT DATE *(DD-MM-YYYY)*	2. REPORT TYPE	3. DATES COVERED *(From - To)*
01-11-2019	Final Performance	15 Sep 2014 to 14 Sep 2018

4. TITLE AND SUBTITLE
State-of-the-Art High-Flux Mono-Energetic Ion Sources Driven by Ultra-Intense Laser Pulses

5a. CONTRACT NUMBER

5b. GRANT NUMBER
FA9550-14-1-0282

5c. PROGRAM ELEMENT NUMBER
61102F

6. AUTHOR(S)
Farhat Beg, Alexander Thomas, Karl Krushelnick

5d. PROJECT NUMBER

5e. TASK NUMBER

5f. WORK UNIT NUMBER

7. PERFORMING ORGANIZATION NAME(S) AND ADDRESS(ES)
UNIVERSITY OF CALIFORNIA, SAN DIEGO
9500 GILMAN DR DEPT 621
LA JOLLA, CA 92093-0621 US

8. PERFORMING ORGANIZATION REPORT NUMBER

9. SPONSORING/MONITORING AGENCY NAME(S) AND ADDRESS(ES)
AF Office of Scientific Research
875 N. Randolph St. Room 3112
Arlington, VA 22203

10. SPONSOR/MONITOR'S ACRONYM(S)
AFRL/AFOSR RTB1

11. SPONSOR/MONITOR'S REPORT NUMBER(S)
AFRL-AFOSR-VA-TR-2019-0315

12. DISTRIBUTION/AVAILABILITY STATEMENT
A DISTRIBUTION UNLIMITED: PB Public Release

13. SUPPLEMENTARY NOTES

14. ABSTRACT
The project State-of-the-art high-flux mono-energetic ion sources driven by ultra-intense laser pulses has made significant progress in the completion of project goals outlined in the original proposal. First, the effects of the laser parameters were examined using both the Hercules and T-cubed lasers at the University of Michigan. This information was crucial to understand how the laser energy is coupled to thin targets, which this project utilizes for the production of ion beams, when ultra-short pulses at high intensity with ultrahigh contrast conditions are used. This work showed that relatively high reflectivities of laser light are achievable at the typically used laser intensities, which is important when plasma mirrors are used to enhance the laser pulse contrast. The effects of surface limited targets on electron dynamics were also examined. This portion of the work also found that smaller surface areas can limit the sheath field development to a localized area, and therefore increase the strength of this accelerating field. Stronger sheath fields then enhance the acceleration of ions. Second, a weak departure from the TNSA ion acceleration mechanism, attributed to contributions by the RPA mechanism, was observed in experiments utilizing the Hercules laser. These experiments showed the production of high-charge-state ion beams with high energy per nucleon, high maximum energy, and narrow energy band concentration when thin (sub-micron thickness) foil targets were used. This work demonstrated the predictive capabilities of the collaboration through the use of the particle-in-cell (PIC) codes EPOCH, while also providing important information for the benchmarking of the codes. The modeling work during this segment of the project also explored extensive parameter space relevant to the optimization of target design for the currently examined laser capabilities, su

15. SUBJECT TERMS
relativistic optics, plasma, ion acceleration

16. SECURITY CLASSIFICATION OF:			17. LIMITATION OF ABSTRACT	18. NUMBER OF PAGES	19a. NAME OF RESPONSIBLE PERSON
a. REPORT	b. ABSTRACT	c. THIS PAGE			STICKRATH, ANDREW
Unclassified	Unclassified	Unclassified	UU		19b. TELEPHONE NUMBER *(Include area code)* 703-696-9511

COVER PAGE

State-of-the-art high-flux mono-energetic ion sources driven by ultra-intense laser pulses

AFOSR-BRI Award #FA9550-14-1-0282

Principal Investigator: Prof. Farhat Beg
Center for Energy Research
University of California at San Diego
Phone: (858)822-3476
E-mail: fbeg@ucsd.edu

Submission Date: March 1, 2019

Recipient Organization: Science & Engineering Research Facility (SERF)
University of California at San Diego
9500 Gilman Drive
La Jolla, CA 92093-0411

Project/Grant Period: 09/15/2014 – 09/14/2018

EXECUTIVE SUMMARY

Intense ion beams accelerated from short-pulse high-intensity lasers have an abundance of applications including nuclear reactions, production of super-heavy elements, ion beam fast ignition fusion concept, radiation effects in materials, and radiation oncology. In order to be useful for these applications, ideal ion beams should have a sub-picosecond duration, micrometer-scale source size, low divergence, and be mono-energetic. Traditional ion acceleration has been realized via the Target Normal Sheath Acceleration (TNSA) mechanism, which typically accelerates protons to high energies (10's of MeV) by utilizing thin (1-100 micron thick) foil targets driven by short, high-intensity (10^{19}-10^{20} W/cm^2) laser pulses. Measurements of the ion spectra associated with this acceleration scheme have also shown the presence of high-energy, low-charge-state heavy ions accelerated along with the proton source. This is not the path forward for the acceleration of mono-energetic heavy-ion beams, however, as the laser energy is most efficiently coupled to protons. This is due to the preferential acceleration of lighter ions through the electrostatic sheath field developed at the rear surface of the target, meaning that little energy is imparted to the heavier ion species. Moreover, this mechanism leads to a weak maximum ion energy scaling with laser energy of $E_{max} \sim I_L^{0.5}$.

The advent of laser systems capable of delivering short (30-700 fs) ultra-high contrast (~10^{15}) laser pulses with intensities in the range of 10^{20}-10^{21} W/cm^2 has enabled the use of ultra-thin (sub-micron) target foils. This allows access to new regimes of ion acceleration including Radiation Pressure Acceleration (RPA), breakout afterburner (BoA), "laser-piston" (LP) and Relativistic Induced Transparency (RIT). Recent theoretical studies have shown that these mechanisms could greatly improve the ion beam quality and maximum obtainable energy in comparison with the TNSA mechanism.

The project State-of-the-art high-flux mono-energetic ion sources driven by ultra-intense laser pulses has made significant progress in the completion of project goals outlined in the original proposal. First, the effects of the laser parameters were examined using both the Hercules and T-cubed lasers at the University of Michigan. This information was crucial to understand how the laser energy is coupled to thin targets, which this project utilizes for the production of ion beams, when ultra-short pulses at high intensity with ultrahigh contrast conditions are used. This work showed that relatively high reflectivities of laser light are achievable at the typically used laser intensities, which is important when plasma mirrors are used to enhance the laser pulse contrast. The effects of surface limited targets on electron dynamics were also examined. This portion of the work also found that smaller surface areas can limit the sheath field development to a localized area, and therefore increase the strength of this accelerating field. Stronger sheath fields then enhance the acceleration of ions.

Second, a weak departure from the TNSA ion acceleration mechanism, attributed to contributions by the RPA mechanism, was observed in experiments utilizing the Hercules laser. These experiments showed the production of high-charge-state ion beams with high energy per nucleon, high maximum energy, and narrow energy band concentration when thin (sub-micron thickness) foil targets were used. This work demonstrated the predictive capabilities of the collaboration through the use of the particle-in-cell (PIC) codes EPOCH, while also providing important information for the benchmarking of the codes. The modeling work during this segment of the project also explored extensive parameter space relevant to the optimization of target design for the currently examined laser capabilities, such as those used in the experiments at the Hercules laser facility (I_o=3x10^{20} W cm^{-2}, 3J, 40 fs). In addition to optimization of thin foil targets, several novel target designs were explored as potential candidates for improving ion energy and flux. Further theoretical work conducted at the Naval Research Laboratory also examined the potential benefits of utilizing drivers with similar intensities and prepulse contrasts, but higher energies, correspondingly higher laser fluence, and longer pulse-lengths.

In experiments on the Trident laser, mono-energetic Ti ion beams of several charge states from 14 to 22 were observed with a maximum number of ions for charge state 20. The target thickness (60 nm to 140 nm) scan showed that the optimum thickness was 100 nm. Mono-energetic Ti ions with energies in excess of 150 MeV were observed. These results were confirmed by particle-in-cell (PIC) simulations, which showed direct acceleration of mono-energetic ions up to charge state 20 with maximum ion numbers for state 20 using EPOCH code.

The modeling work during this segment of the project explored an extensive range in parameter space relevant to the optimization of target design for the currently available laser systems, such as the Texas Petawatt laser (TPW) at the University of Texas Austin, the Bella Laser at the Lawrence Berkeley National Laboratory and the Titan laser at the Lawrence Livermore National Laboratory. These lasers cover a wide range of energies and pulse lengths implying that different ion acceleration mechanisms can be observed. This work represents major progress in the understanding of the physics associated with ion beam acceleration by ultra-relativistic laser pulses.

NARRATIVE

1. Introduction

Some of the prime interests in the relativistic laser-plasma interaction field are compact sources of high-quality energetic particles (electron and ion) having ultra-short durations. Specifically, heavy-ion beams are vital to multiple applications [1-4], including the production of super-heavy elements and exotic isotopes [5,6]. However, the vast majority of published experimental data have been limited to measurements of light ions.

The most-studied ion acceleration mechanism, Target Normal Sheath Acceleration (TNSA) mechanism [7-10], is very robust and was shown to generate reproducible exponential energy spectrum of light-ions originating from the contaminants located at the target rear-side. TNSA typically accelerates protons to high energies (10's of MeV) by utilizing thin (1-100 micron thick) foil targets driven by short, high-intensity (10^{19}-10^{20} W/cm^2) laser pulses. Measurements of the ion spectra associated with this acceleration scheme have also shown the presence of high-energy, low-charge-state heavy ions accelerated along with the proton source. This is not the path forward for the acceleration of mono-energetic heavy-ion beams, however, as the laser energy is most efficiently coupled to protons. This is due to the preferential acceleration of lighter ions through the electrostatic sheath field developed at the rear surface of the target, meaning that little energy is imparted to the heavier ion species. Moreover, this mechanism leads to a weak maximum ion energy scaling with laser energy of $E_{max} \sim I_L^{0.5}$.

Among the numerous ion acceleration mechanisms identified to date, the most promising for producing high-energy heavy-ion beams is the Radiation Pressure Acceleration (RPA) mechanism. This novel mechanism has aroused extensive theoretical attention in recent years [11-14] due to a rapid progress of high-contrast high-intensity laser technology mentioned above. A high-intensity laser can exert an enormous radiation pressure (60 Gbar at 10^{20} Wcm^{-2}) at the reflection point on a foil surface, which results in local electron-ion displacement and ion acceleration via the ensuing space-charge field. If this charge-separation field is strong enough to accelerate ions quickly to velocity comparable to the electrons, the distance between the electrons and ions will remain relatively small, and instabilities will not have time to develop. Therefore, the ions and electrons moving together represent a relativistic mirror co-moving with the laser pulse, as in the 'light sail' (LS) paradigm. Cyclical acceleration of the target ions in the LS RPA mode accessible with thin foils is predicted to lead to highly energetic, narrow-band ions.

The main reason RPA is currently attracting a substantial amount of experimental and theoretical attention is the predicted superior scaling of ion energy with laser intensity, $E_{max} \sim I_L^{5/3}$. Recent experimental work has shown an increase in heavy ion energy when very thin (35-500 nm) targets were driven by high-intensity (10^{20} W/cm^2) and ultra-high-contrast (10^{13}) laser pulses from the HERCULES laser, produced light ion (Si, N, C, O) ion beams with maximum energies of 2-3 MeV/nucleon [15].

Another promising mechanism is Relativistically Induced Transparancy (RIT) [16-19]. When the main pulse (> 10^{20} W/cm^2) interacts with the ultrathin foil, the expansion and laser heating of the plasma can cause the maximum electron density to rapidly decrease, allowing light to propagate further inside the target, causing the occurrence of RIT. The onset for this transparency regime is limiting the foil boost for the RPA mechanism, but can however lead to efficient ion acceleration via volumetric heating of the electrons as the target becomes transparent, therefore efficiently accelerating ions from the bulk material volume. Our work shows that, the transparency onset also leads to the development of self-organizing field structures at the target rear-side when the laser breaks through the target, that we further identify in

our simulations to play a major role to accelerate the heavier ions with low divergence and narrow spectral peaks.

2. Project Milestones and Achievements

I. Optimization of Target and Driver Properties for Ion Beam Acceleration

a) *Trends in high intensity laser absorption at oblique incidence angles for solid density targets*

Recently, large advances have been made in ultra-short pulse lasers (pulse length ~ 30fs), where repetition rates and pulse energy are continuously pushed upward. These lasers enable the investigation of the so-called “ultra-relativistic" regime, in which the laser electric field is far beyond what is necessary to accelerate an electron to relativistic velocities. Several experiments have been performed recently with peak intensities in excess of 10^{21} Wcm^{-2}. Laser-solid interactions at these intensities have a host of interesting applications including laser driven ion acceleration, extreme ultraviolet and x-ray generation, and neutron generation.

A laser interacts strongly with a plasma at the critical density, the point at where the laser frequency is equal to the plasma frequency. At electron densities below the critical density the plasma is transparent, otherwise it is opaque. At ultra-relativistic intensities, the laser imposes a substantial radiation pressure on the plasma, and may displace the plasma, i.e., “hole-boring." The electrons respond much faster than the relatively massive ions, so an electrostatic restoring force occurs if the electrons are displaced. However, for sufficiently thin plasmas the radiation pressure may surpass this restoring force and begin to accelerate the entire plasma, commonly known as the laser piston or radiation pressure acceleration (RPA) regime.

Although laser technology advances, there is still substantial difficulty in performing an experiment at these regimes. Critically, the density profile of a solid density target is rarely well characterized or controlled causing substantial variations in the amount of laser energy absorbed and hot electron production. This preformed plasma is generated from laser prepulses that are unavoidable in modern laser systems. The amplified spontaneous emission (ASE) is a nanosecond duration pulse that causes hydrodynamic expansion of the target, resulting in an exponential preplasma density profile that typically extends many microns into the vacuum. For ultrathin targets, this can lower the density substantially, even to the point of being below the critical density. The ratio of laser intensity between the main pulse and these prepulses is known as the “laser contrast." Since the laser focus is typically Gaussian-like the plasma profile is not uniform spatially across the focal diameter which causes significantly higher laser absorption.

In this part of our project, we showed the effects of hole-boring deformation as well as radiation pressure deformation on solid foil targets through reflectivity at oblique incidence angles. Ultrahigh contrast is used to mitigate the effects of laser prepulse. Laser reflectivity is found to stay near constant as the target is brought into focus to ultra-relativistic intensities, with S-polarized reflectivity being substantially higher than P-polarization. However, for thin targets where radiation pressure can deform the plasma, reflectivity drops in both cases to a few percent. The thin targets were studied with 3-dimensional particle-in-cell (PIC) simulations, which demonstrate dramatic target deformation along with a drop in reflected power that is consistent with what is observed experimentally.

The experiments were performed using the HERCULES laser facility at University of Michigan, a Ti:Sapphire system (λ = 800 nm) producing laser pulses with t = 40 fs duration full-width at half-maximum (FWHM) and an ASE intensity contrast of 10^{-11}. Prior to the experimental chamber, mirrors in a secondary chamber focus the amplified pulse onto a pair of antireflection coated BK7 glass substrates that act as plasma mirrors. Each plasma mirror reflects < 0.15% of S polarized light at 810 nm while possessing a measured reflectivity of 65%-70% at high intensity, producing a ns-level ASE contrast of < 10^{-15}. This contrast improvement should prevent preplasma formation until 1 ps before the main pulse interaction, so that the density profiles remain extremely sharp. After the plasma mirrors, a Mica 1/2 waveplate enables changes the polarization (between S and P). Beam profile monitors recorded the near and far field patterns of the beam after the waveplate to verify focal spot quality, and to confirm that the 2 waveplate did not noticeably increase the pulse length.

In this experiment, the laser delivered 1.5 joules to the target with 55% of the energy in a 1.2 µm FWHM focal spot via an f/1 off-axis parabolic mirror (OAP). This results in an on-target intensity of 2 x 10^{21} Wcm^{-2} ($a_0 = 30$). A near diffraction limited spot size with a Strehl ratio of 0.6 was attained by using a deformable mirror (Xinetics) and a Shock-Hartmann wavefront sensor, which are used to correct aberrations predominantly from the OAP. The beam diameter was 10 cm.

The targets used in the experiment were free standing silicon nitride membranes (SiN) with thicknesses of 30-100 nm, 1 µm Mylar ($C_{10}H_8O_4$) foils, and polished silica and fused silica. The targets were positioned at the laser focus with an accuracy of ~2 µm (half of the Rayleigh length) at an incidence angle of 45 degrees. A P-I-N diode with a 25 µm Be Filter and a dipole magnet in front measured x-ray emission above 2 keV from the interaction region on the front side of the target. A sodium iodine detector and a plastic scintillator was used with 10 cm of lead shielding to look at high energy x-rays from the interaction.

Laser light was reflected to a white scattering screen positioned 10 cm from the interaction, equivalent to a focal length. This screen was imaged onto a CCD with calibrated neutral density filters and an interference bandpass filter to examine the reflected 800 nm light. The screen was calibrated with low-energy pulses and a calorimeter. A beamsplitter prior to the CCD sent light into an optical spectrometer. A small hole in the screen was present to enable measurement of the extreme ultraviolet emission with an x-ray spectrometer. A transmitted light screen was also present, however, large scattering from the Au coating of the OAP increased the noise threshold of the screen to approximately 5%.

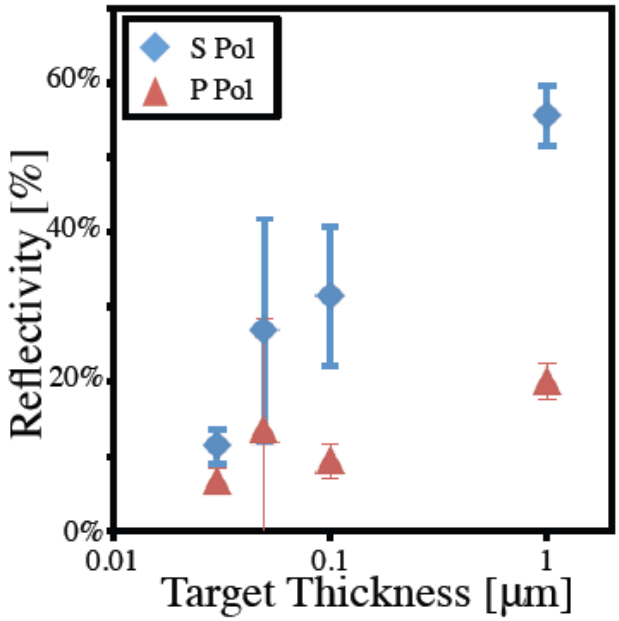

Figure 1. *Reflectivity as a function of target thickness for multiple targets for S polarization (blue diamonds) and P polarization (red triangles). Targets with thickness 1 µm or larger are considered "bulk" and are represented by the 1 µm data point, since reflectivity did not change beyond this thickness.*

Reflectivity for targets ranging from 1 µm to bulk targets with mm thickness were consistent across materials and are plotted in Fig. 1, with S and P polarized light reflecting 56% and 20% of the fundamental, respectively. Reflectivity was found to be weakly dependent on intensity, with reflectivity for both polarizations increasing by roughly 10% as the target was moved out of focus. The beam profiles for S polarization were clear and sharp and closely resembled the beam at low intensity, as shown in Fig. 2. Small, mm sized damage spots in the coating of the deformable mirror can be clearly observed in the reflected beam profile. In the P polarization case, the reflected beam profile showed heavy modulation in the amplitude and the spatial shape that varied shot to shot. An example profile is shown in Fig. 2.

The reflectivity dropped substantially as the target thickness decreased, as shown in Fig. 1. S polarized reflectivity dropped to 11% for 30 nm targets, while the reflectivity dropped to 7% for P polarization. Higher error bars exist for 50 nm targets since only two shots were performed there.

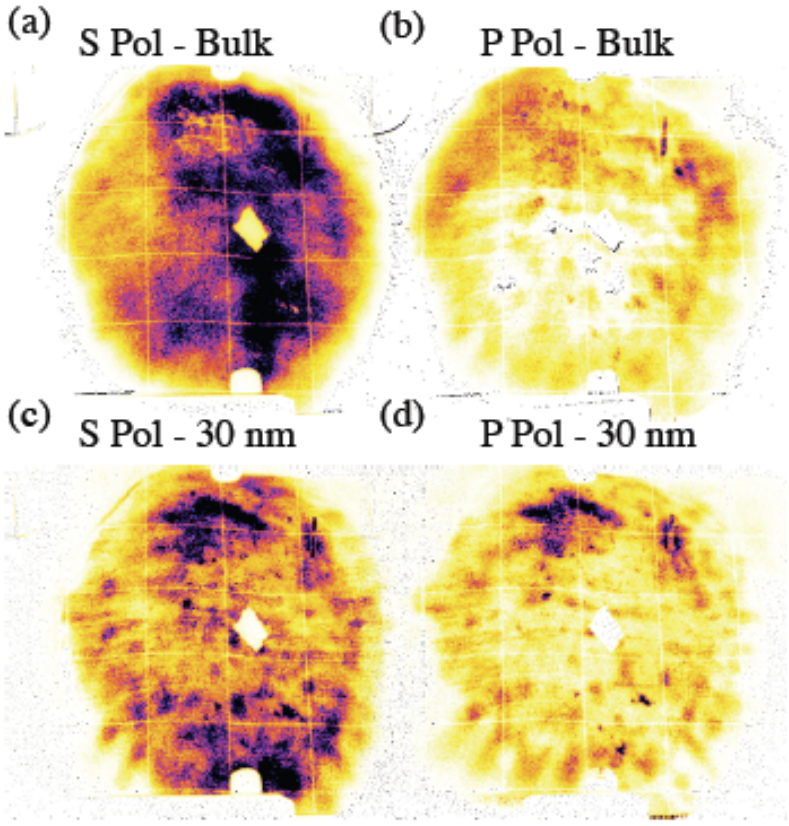

Figure 2. *Reflected beam profiles for Si Wafer targets at S (a) and P (b) polarizations, and for 30 nm SiN targets at S (c) and P (d) polarizations. The color scales are the same for the bulk targets and are scaled 5 times higher for the SiN targets. The screen extends to the edge of the frame.*

In addition, the beam profile for both polarizations presented significant modulation that varied shot to shot as shown in Fig. 2. Though modulated, the beam profiles did have a well-defined diameter. There was no change in the signal observed in the transmitted light screen, though the screen was not present for all shots. No high harmonic signal was observed for either ultrathin targets or S polarization and for the ultrathin targets no blackbody continuum was observed. However, the Oxygen V emission line was observed to both broaden and redshift for the ultrathin targets. All targets showed comparable signals for the scintillator detectors, though for the ultrathin targets both polarizations generated a signal ~ 5 times weaker on the PIN diode than for the thicker targets.

The reflectivities at thicker targets are consistent with lower intensity studies performed, such as the case for plasma mirrors. Using plasma mirrors as a pulse cleaning optic has an upper limit on intensity due to the finite laser contrast that exists natively in the laser, which causes preplasma prior to the main pulse. Nevertheless, increasing the laser contrast minimizes preplasma, and in turn minimizes the amount of plasma that exists below the critical density that the laser may interact with and be absorbed by. For very high contrast, scale lengths on the order of tens of nm may be achieved, which is thin enough to suppress high harmonic generation. Indeed, a very uniform surface must be present at the focus to maintain high frequency noise in the reflected beam profile such as the damage spots which are 1/100th the diameter of the beam. Besides, with S polarization the electron absorption is minimized.

The reflectivity rapidly decreases with thickness. The lack of blackbody continuum combined with the weaker signal on the PIN diode clearly demonstrates the lack of thermal electrons from the thin targets. The consistent signal from the scintillator detectors imply that high energy electrons generated at the focus are still generated, and previous experiments with similar geometry and targets demonstrated a rise in the maximum ion energy when decreasing target thickness. Preplasma generated by laser contrast is expected to be similar to what is observed for bulk targets, and particularly in the case of S polarization another energy absorption mechanism is needed to explain such a loss of energy.

The redshift of the Oxygen V emission line also provides some insight. Oxygen originates from the hydrocarbon contaminants such as water that adhere to the surface of nearly every target, and thus provides a means of determining the motion of the target surface. For such thin targets, the laser is able to accelerate the entirety of the target during the pulse duration. The finite focusing, however means that there is varying acceleration across the diameter of the focus, with the target outside of the focal diameter remaining stationary. This necessitates a deformation of the target, which removes the ability to model the target as a one dimensional system. Previously, numerical simulations have studied the role of target

deformation with regards to absorption and electron transport.

The targets in this experiment are initially smooth and unperturbed, but the ultrahigh intensities may rapidly perturb this condition. Consider Brunel heating, in which the electrons move in the intense laser field a distance of v_{osc}, where v_{osc} is the electron quiver velocity and for $a_0 \sim 1$ is approximately c, the speed of light. For an oblique incidence angle with P polarization, the electrons will move in and out of the plasma. For solid density plasmas where the skin depth is much smaller than this distance, the electrons are removed from the laser field and cannot return, taking energy away from the laser field. For S polarization, electron motion is in plane and Brunel heating cannot take place. This is the reason why the reflectivity is globally higher for S polarization, as shown in Fig. 2.

Intense laser pulses impart a strong pressure on the plasma. Several previous studies have presented a one dimensional model based on the balance between the radiation pressure force and the electrostatic force from separating electrons from ions. For bulk targets, solid density plasmas are able to provide a substantial force that prevents deformation, whereas in thin foils the electrostatic force may be overcome due to the finite number of ions and electrons. From previous work, an expression for the energy per nucleon of ions in a plasma undergoing radiation pressure acceleration is given by

$$E_{ion} \approx 2\pi \frac{Z m_e a_0^2 \tau}{A m_p \zeta}$$

where Z is the ionization state, A is the atomic mass, τ is the number of cycles in the laser pulse, and m_e and m_p are the masses of the electron and proton respectively. ζ is the surface density of a plasma with thickness d and electron density n_e, and is given by $\zeta = \pi \frac{n_e d}{n_c \lambda_0}$. This model assumes a flat top pulse and 100% reflectivity, and is non-dissipative.

The very center of the focal diameter is where the model most accurately describes the interaction of this experiment. A fully ionized SiN target has a density of 532 n_c, and the laser intensity of $a_0 = 30$ will accelerate a target of 30 nm up to 46 MeV. At a radius of 0.6 μm away from the center of the focus, the intensity has dropped such that the target is moving at an order of magnitude lower velocity. The angle between these two points should climb to 57.5° by the end of the pulse, if the absorption is neglected. However, since this deformation is symmetric, it enables S polarization to become P, and Brunel absorption can take place. Midway through the pulse the angle induced is 22.9°, which implies Brunel absorption of 18.9%.

This crude model highlights the physical possibility of radiation pressure induced absorption, though many assumptions are made. To further demonstrate the mechanism of deformation, 3D PIC simulations were performed using the OSIRIS code. 3D simulations were necessary for this geometry, since in 2D the target is unable to deform out of plane and all

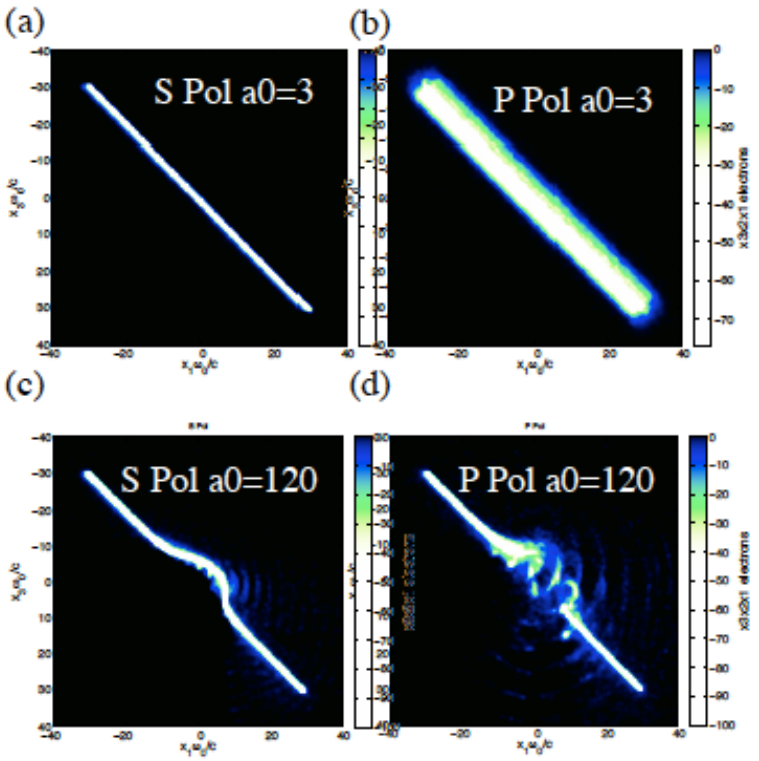

Figure 3. *PIC simulations of electron density at the end of the pulse for a 120 nm target with low intensity of $a_0 = 3$ for S (a) and P (b) polarizations and for high intensity of $a_0 = 120$ for S (c) and P (d) polarizations. Substantial deformation is observed at large intensities.*

light is S polarized. The computational requirements for 3D simulations are extremely high, so an analogous situation was simulated in order to be performed with finite resources. In the following simulations, fully ionized carbon targets with thickness 120 nm and density of 500 n_{crit} and a scale length of 12 nm were used to match experimental conditions. A laser pulse with duration 15 cycles had varying intensities with a_0 = 1 to 120 at a 45° angle of incidence and a 1.5 μm diameter focal spot. The pulse shape is a fifth order polynomial in time and a Gaussian in space. Runs were performed both with and without ion motion. The cell size was 31.8 nm in each axis, with 64 particles per cell for electrons and 8 particles per cell or ions. Simulations were performed with both S and P polarizations.

At low intensities, approximating thick targets in the experiment, little deformation is observed in the target for both polarizations, as shown in Fig. 3. S polarization shows a total energy reflectivity of 98% while P polarization reflects 80%. As intensity increases, the reflected energy drops, and an increase in electron temperature is observed along with increased deformation. At intensities of a_0 = 120, deformation is substantial, and the reflected energy drops by a total of 30% for S polarization and 20% for P polarization. In fact, at these higher intensities, the electron temperatures are comparable between S and P polarization, as shown in Fig. 4. In none of the simulations there was transmitted light with energy greater than 1% of the incident pulse.

It is important to note that the total energy reflected is not the same as the experimentally observed fundamental reflectivity, which only examines light in a narrow band around the fundamental. Also, electron collision dynamics are not modeled in PIC, so absorption is lower than what it is in reality. However, the relative drop in reflected energy is consistent with what is observed experimentally. Additionally, the lack of transmitted light means that the target was not transparent, so that the mechanism does not rely on the laser boring through the target or entering the relativistically transparent regime, in which the relativistic mass of the electrons effectively lowers the density of the plasma to the point of it being below the critical density. Though bulk targets have a substantial electrostatic force mitigating deformation, it still may occur and offers an explanation to why small drops in reflectivity occurs at these strongly relativistic intensities.

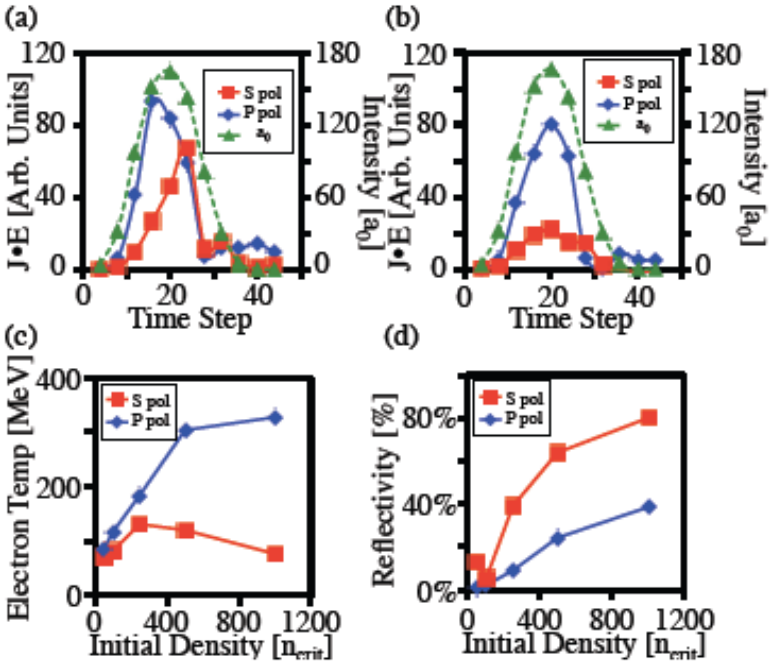

Figure 4. *3D PIC simulations for S (red squares) and P (blue diamonds) polarization. The work performed by the laser is shown as a function of the simulation timestep (1.5 fs) for an initial density of 250 n_{crit} (a) and 1000 n_{crit} (b). Also shown is the laser envelope as a function of time step (green triangles). The electron temperature at the end of the simulation as a function of initial density is shown in (c). Reflected fundamental is shown as a function of initial density in (d).*

In conclusion, experiments were performed to investigate the absorption of ultra-short pulses at high intensity with ultrahigh contrast conditions. We discovered that trends in absorption done at lower intensities are consistent even into the strongly relativistic regime, where at intensities surpassing 10^{21} Wcm^{-2} relatively high reflectivities are achievable. This bodes well for experiments that rely on plasma mirrors that are close to the interaction site. However, it was observed that the reflectivities dropped substantially for thinner targets due to radiation pressure induced deformation. 3D simulations show the deformation and corresponding absorption even with S polarization, which is commonly used to minimize electron heating and increase reflectivity. Investigations into even higher intensities will need to discover means of controlling the

target motion across the focus during the pulse in order to explore new regimes, otherwise electron heating will dominate before the peak intensity may be reached.

b) ***Surface Limited Target Effects on Electron Dynamics with Femtosecond Laser Plasma Interactions***

Understanding the propagation of energetic electrons from short-pulse laser matter interactions with solid density targets is critical for understanding these plasmas. The electron induced sheath field has been observed to extend millimeters from the interaction point in foil targets. As the sheath extends across the target surface the field strength decreases. Confinement of the sheath to a target with a limited surface area has the potential to increase the field strength, and therefore the proton energies.

Mass limited targets have previously been used to increase the strength of sheath fields by decreasing the volume of the target and thereby increasing the hot electron density within the target [20]. Refluxing, or recirculation, of electrons in thin foil targets has been shown to increase electron and proton energies [21, 22]. Computational studies have also predicted new acceleration mechanisms in spherical mass limited targets leading to the generation of quasi-monoenergetic proton beams and electron beams [23].

In short pulse interactions, hot electrons primarily move along surfaces, as a result of confining electric fields, and lose energy to the fields. Computational studies have investigated the effect of mass limited targets on the strength of sheath fields for pulse durations long enough to allow transversal electron recirculation leading to enhanced ion acceleration from additional acceleration of electrons. Improved conversion efficiency and enhanced proton energies have been observed in experiments with laser pulse durations of 100's of fs. For laser pulse durations of 10's of fs enhanced proton energies have been predicted as a result of the concentration of hot electrons. However, this has not been observed experimentally, which has been attributed to preplasma formation effects on small targets due to insufficient laser contrast.

While it is straightforward to simulate an isolated, limited mass target, it is quite difficult to reproduce this situation experimentally. To date, approaches have included suspending small targets on glass stalks or ultrathin wires, and using micron scale droplets. While the benefits of mass limited target would be highly desirable, the use of more traditional targets would be beneficial for applications. Here we consider the effect of controlling the surface area of the targets, without limiting the target mass through isolation, and observe the effects of the changing the ratio of the surface area to the target volume.

The experiment was performed using the HERCULES laser facility. As mentioned above, HERCULES is a Ti:sapphire system (λ = 800 nm) producing laser pulses with 40 fs duration full width at half maximum (FWHM) with an amplified spontaneous emission intensity contrast of 10^{-11}. The laser delivered 1.4 J to the target at normal incidence in a 2.7 μm FWHM focal spot via an f/3 off-axis parabolic mirror. This resulted in an average on-target intensity of 6.1 x 10^{20} W/cm^2 (a_0 = 17). A near diffraction limited spot size with a Strehl ratio of 0.6 – 0.8 was attained by using a deformable mirror (Xinetics) and a Shack-Hartmann wave front sensor. The HERCULES laser operates at a 0.1 Hz repetition rate. For the purpose of comparison, one image is shown from the T-cubed laser which has a longer, 400 fs, pulse duration. The T-cubed laser delivered 7.2 J to the target in a 5 μm FWHM focal spot, which resulted in a focused intensity of 4.5 x 10^{19} W/cm^2 (a_0 = 5). This data point illustrates the effects of lower intensity with longer pulse duration.

In this section, we present results from foil, wire, and mesh copper targets. The foil target was 12:5 μm thick. The mesh targets were square and hexagonal girds purchased from SPI supplies. The square mesh had a 62 μm pitch with 8 μm bar width and was measured to be ~ 9 μm thick. The hexagonal mesh had a 83 μm pitch with a 10 μm bar width. The wire target diameters ranged from 185 to 15 μm. The effect of different target shapes was measured by varying the target geometry while maintaining approximately the same target thickness. Transverse alignment of the mesh and wire targets required few micron precision to overlap the focal spot and the 8 μm width mesh bars. This was accomplished by imaging the location of the focused low energy regenerative amplifier laser seed pulse on the target.

The primary ion diagnostic was CR-39 located normal to the target on the rear side. Mylar filter stacks were used to measure proton flux in multiple energy bins, allowing the measurement of a proton

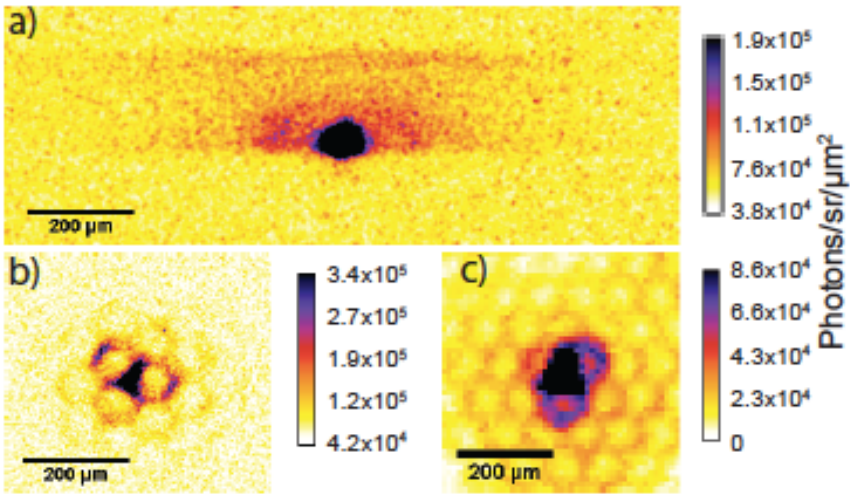

Figure 5. *Cu K-alpha images of wire (a) and hexagonal mesh (b,c) targets. The current was observed to flow on the surface of the 185 µm wire (a), producing enhanced edges in the K-alpha image. Identical mesh targets shot on the 40 fs HERCULES laser (b) and 400 fs T-cubed laser (c) showed qualitatively different electron behavior. In the higher intensity interaction, asymmetric electron current around the hexagonal loop (b) was attributed to field induced current along parallel wire segments. In contrast, a symmetric current was observed around the hexagonal loops in the lower intensity interaction (c).*

energy spectrum. Each bin acted as a high pass filter yielding a proton signal above the energy cut-off. CR-39 was placed at distances of 1 or 5 cm from the target to measure the proton beam profile or 45 cm from the target to measure the energy and flux.

Cu K-alpha emission from the targets was imaged using a spherically bent Quartz [2131] crystal with a 2d = 3.082 A lattice spacing. The crystal, which had a 400 mm bending radius, was placed 242 mm from the target and produced an image at 1260 mm, yielding a magnification of 5. An Andor iKon-M BR-DD was used to detect the imaged photons. The CCD had 13 µm pixels and a quantum efficiency of 45% at the Cu K-alpha energy. The imaging system was aberration limited to a resolution of 15 µm with a 25:4 mm aperture. The absolute photon yield was calculated using the manufacturer specified CCD response and crystal's integrated reflectivity.

The Cu K-alpha images measured the relative magnitude and location of hot electrons within the target material as shown in Fig. 5. Edge-enhancement of the Cu K-alpha signal in Fig. 5(a) demonstrated that the current was on the surface of the 185 µm wire. This provided experimental corroboration of simulations of laser induced electron transport in 40 µm wires, which had predicted the bulk of the current traveled along the wire surface. In Fig. 5(b) and (c) the Cu K-alpha signal from identical hexagonal mesh targets shows distinct differences between the HERCULES (b) and T-cubed (c) shots. The higher intensity HERCULES shot shows an asymmetry as the current is traced along hexagonal loops, with an enhancement of the current in parallel wire segments. Alternatively, the lower intensity and longer pulse duration T-cubed shot shows isotropic current flow around the wire hexagons. This suggests that the lower intensity interaction drives a direct current in the target, while the higher intensity drives an induced current through strong, rapid electric and magnetic field growth. It is worth noting that the higher energy of the T-cubed laser also led to Cu K-alpha illumination of a larger extent of the hexagonal mesh, however in the HERCULES and T-Cubed shots the photon flux per Joule was found to be 1.1 x 10^9 and 1.3 x 10^9 photons/sr/J, respectively.

The effect of limiting the target surface was measured using foil, mesh, and 15 μm wire targets on HERCULES, as shown in Fig. 6(a)(b)(c). The total Cu K-alpha was remarkably consistent between targets, varying from 9.5 x 10^9 to 1.1 x 10^{10} photons in the three images in Fig. 6, which is consistent with laser shot-to-shot fluctuations. The total conversion efficiency into Cu K-alpha was 1 x 10^{-5}, consistent with previous results.

Previous studies of the effects of reduced volume on Cu K-alpha yield have shown a reduction in K-alpha yield for lower volume targets. This was partially attributed to broadening and shifting of the K-alpha emission as a result of heating. However, this was observed for longer pulse durations (10 ps) and higher pulse energies (>75 J) than in the present experiment, for the same volume targets, which would lead to more target heating. A reduced K-alpha signal was not observed for the investigated targets, indicating the target heating was insufficient to alter the K-alpha emission.

The confinement of K-alpha signal in the mesh and wire targets led to a higher signal density since approximately the same total Cu K-alpha signal was observed for the targets with smaller surface areas. The vertically and horizontally integrated profiles (d) of the images shows the wire and mesh had very similar horizontal profiles. The mesh target had higher signal along the vertical segments and lower signal in between. The horizontal profile of the wire was similar to the profile of the foil since the electron was unrestricted in the horizontal direction. However, the vertical profile shows strong confinement of the wire signal. This was an important result because it showed that although the conversion efficiency of electrons into each target was approximately the same, the differences in target surface area constrained the electrons leading to increased electron density in the reduced surface area targets. The observation that the spatial extent of the Cu K-alpha was approximately equal for each target indicated the hot electrons lost their energy to the fields, as opposed to collisions within the target.

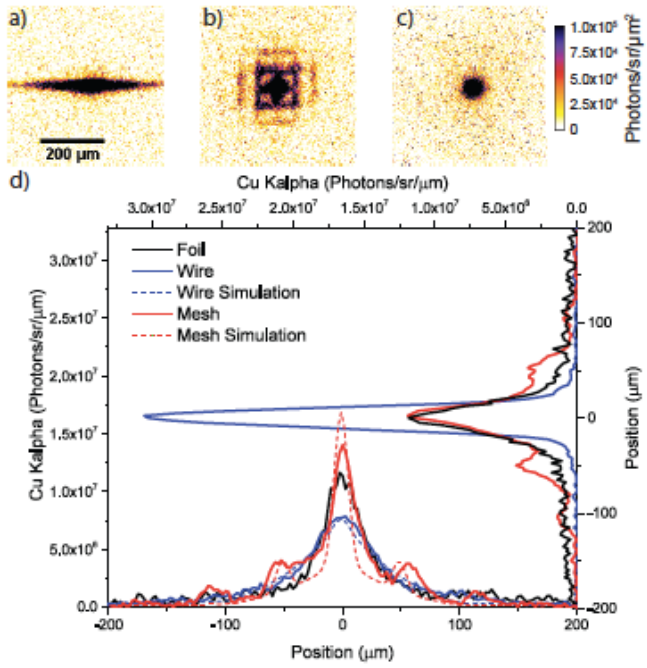

Figure 6. *Cu K-alpha images of (a) wire (b) square mesh and (c) foil targets. The confinement of electrons due to the target geometry leads to strong electron currents that illuminate the target. Vertically and horizontally integrated profiles (d) of the images show how the signal is distributed. Dashed lines represent the scaled simulation results and show excellent agreement.*

The proton spectra provided a direct measurement of the electron sheath field. The proton spectra, shown in Fig. 7, were well characterized by exponential fits. The effective temperature of the spectra increased as the target surface area was reduced from the foil to the mesh to the wire. This result indicated that as the electron sheath was confined to a smaller area the field strength increased, accelerating protons to higher energies.

While the effective temperature demonstrated a clear trend, the total proton flux was lowest for the mesh target and approximately equivalent for the foil and wire targets. As the surface area of the target decreased it was expected that, while the sheath fields were stronger in magnitude, the area from which protons are accelerated would also decrease, and thus the number of protons would decrease. While this partly explains the mesh data, a reduced flux was not observed for the wire target. The expected reduction in flux for the wire target was counteracted by an azimuthal magnetic field which created a line focus in the proton spatial distribution, as shown in Fig. 8(b). The line focused protons were observed 1 cm and 5 cm from the target, with the same 7° full-width-full-angle vertical divergence. This focused divergence was considerably smaller than the full beam 54° full-width-full-angle divergence for the protons that were not focused. It was also much smaller than the 40° full-width-full-angle proton beam observed from at targets. The focused protons were sampled for the energy spectra.

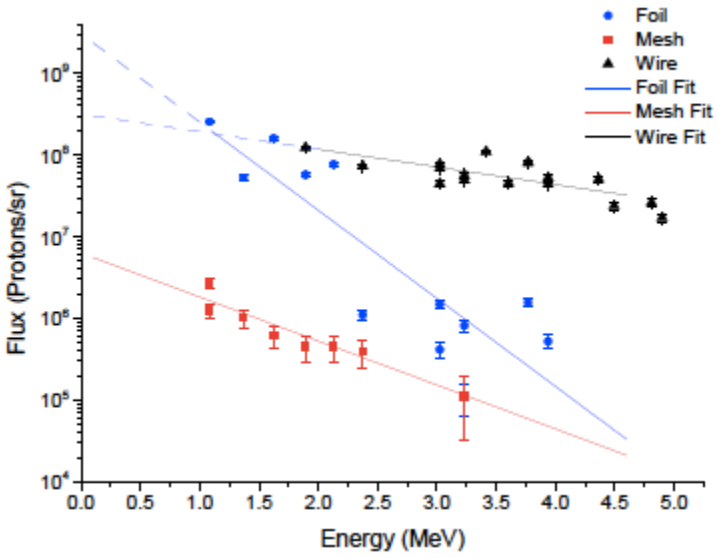

Figure 7. *Ion spectra from (triangle) wire (square) mesh and (circle) foil targets. The values represent the flux of protons above the threshold energy for the filter stack. The slope of the lines of best fit decrease from the foil to the mesh to the wire target. The dashed portions of the fits continue to higher than the saturation point of the CR-39 detector.*

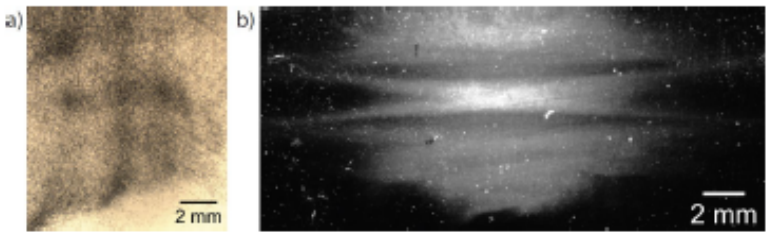

Figure 8. *Microscope image of CR-39 located 1 cm from a mesh target (a) showing mesh pattern in the proton distribution. Scan of CR-39 from a wire target (b) showing a line focusing feature in the proton distribution 1 cm behind the target. The orientation of the focused line was perpendicular to the orientation of the wire target. This feature was also observed 5 cm behind the target with the same angular divergence.*

The target mesh pattern was observed in the proton flux on CR-39 placed 1 cm behind the target, as shown in Fig. 8(a). This image was interesting because it confirmed that the electrons that produced Cu K-alpha on neighboring segments of mesh around the focal spot were also accelerating protons. Additionally, it confirmed that the extent of the Cu K-alpha signal was approximately the extent of the sheath field that contributed to proton acceleration.

To help understand the experimental results simulations were performed for the wire and mesh target geometries using the hybrid Vlasov-Fokker-Planck code, Fido25. Excitation of K shell vacancies was calculated from collisions between the fast electron population and the background. The simulation domain consisted of a box of dimensions L_y = 100 μm by L_x = 200 μm in a 2D slab geometry. The copper targets were represented by piecewise hyperbolic tangent functions. The initial temperature of the bulk target was $k_B T_e$ = 400 eV. The boundary conditions were reflecting and the last few grid points had an exponentially increasing step size.

An isotropic population of electrons were injected into a 5 μm region at the center of the domain with a full width at half maximum temporal duration of 40 fs. The electron beam momentum distribution was defined as a shifted Gaussian with center momentum $p_0 = \left(\sqrt{1+a_0^2}-1\right) 2m_e c^2/3$. a_0 was chosen to be representative of a laser with an intensity of $2\text{x}10^{19}$ Wcm^{-2}, but with a larger focal area in order to match the laser energy from the experiment, with the injected electron beam number density being

calculated using the effective laser energy with an assumed 0:3 absorption fraction.

An azimuthal magnetic field was observed around the wire target, as seen in Fig. 9(a). The field switched orientations around the interaction point due to the change in current directions. This field geometry was consistent with the observed proton focusing. In the grid target azimuthal fields were also observed (b). However, the crossing segments broke up the collective focusing structure.

The spatial extent of the fields was also observed to be consistent between the wire and the mesh, as observed experimentally. The wire target electric field strength, shown in Fig. 9(c), peaked at 2.9 x 10^{11} V/m, while the mesh target maximum, shown in Fig. 9(d), was only 2.2 x 10^{11} V/m. The higher wire field strength was consistent with the experimentally observed wire proton temperature increase. The electric field structure also provided insight into the different proton fluxes observed from the two targets. The laminar field structure around the wire target led to efficient acceleration of protons. Conversely, the low proton flux from the grid targets could be partially attributed to the complex field structure, around the intersection points, which could accelerate protons in a wider divergence angle than the other two targets.

In conclusion, proton acceleration has been studied using structured targets with reduced surface areas. All targets were observed to produced nearly the same total K alpha photon yield over approximately the same spatial extent, indicating the hot electrons were slowed by the fields. The profile of the grid target was observed in the accelerated proton beam profile. This confirmed that the sheath field extended over the same region that produced the K signal. A comparison between the HERCULES and T-cubed shots suggested the higher intensity interaction led to field-induced current flow, which illuminated parallel wire segments, while the lower intensity interaction led to a uniform flow of current along the wires.

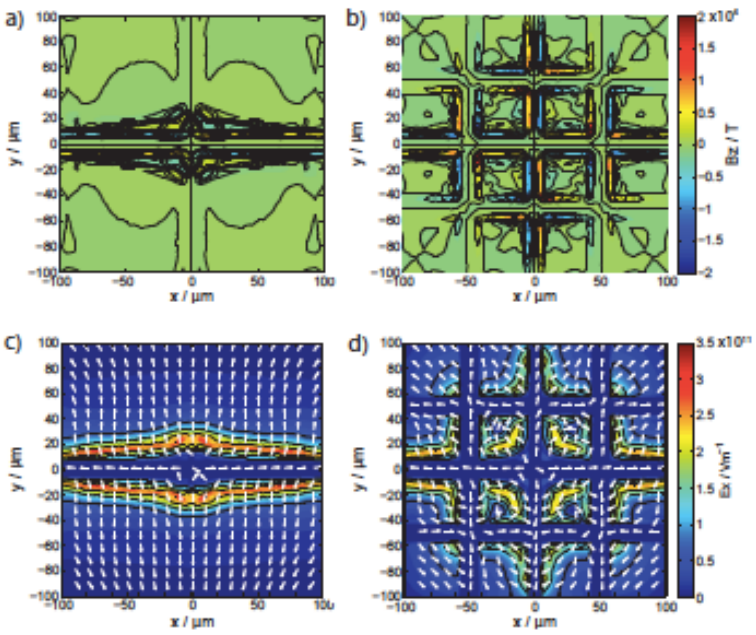

Figure 9. *Data from Vlasov-Fokker-Planck simulation for representations of (a,c) wire and (b,d) mesh targets. The (a,b) magnetic fields are shown at 500 fs and the (c,d) electric fields are shown at 600 fs . Arrows indicate the direction of the electric fields.*

The hot electron density increased as the target surface area was reduced and was correlated to an increase in the sheath field strength, which also increased the temperature of the accelerated proton beam. The increase in sheath field strength was also observed in simulations. The low proton flux observed with mesh targets was attributed to the complex field structure around the intersection points, and the reduced target surface area. Focusing of proton beams was observed from the wire target. Simulations suggest the focusing was the result of azimuthal magnetic fields that resulted from the surface current. In the grid target the field symmetry was broken by the crossing segments and no focusing was observed.

These results have several potential implications for laser plasma accelerators. The increased proton energies, without the use of complex mass limited targets, could be used to enhance proton energies without the need for higher energy lasers. The focusing effect could lead to higher proton beam flux, which could lead to more efficient proton accelerator applications. The use of targets with small surface areas pairs well with femtosecond lasers which typically achieve high focal intensity through sharp focal optics and few-micron-scale focal spots.

II. Experimental Validation of the RPA Scheme for Ion Beams

a) *Acceleration of high charge-state target ions in high-intensity laser interaction with sub-micron targets*

Recently, a weak departure from the TNSA ion acceleration scaling has been observed in experiments performed on the production of light-ion beams (Z<20), which has been predicted by theoretical studies, and is discussed further below. In this work, ultra-thin (sub-micron) foils were driven by ultra-short (40 fs FWHM), high-contrast (~10^{13}), high-intensity (peak intensity ~$3x10^{20}$ Wcm^{-2}) laser pulses. Thin flat-foil targets (50-1300 nm) of various materials were driven by these pulses, and showed the production of ion beams. The ion beams were seen to be predominately comprised of protons when the thicker targets were used, with a transition to heavier ion (Si, C) acceleration as the target thickness was decreased. Although a full transition to RPA dominated acceleration was not observed, it was shown that a regime in which TNSA was not the only mechanism present was demonstrated, and the results are promising for upcoming heavy-ion (Z>20) beam acceleration experiments (discussed in Section IV).

The large energy contrast between the laser main- and pre-pulse was achieved by utilizing two plasma mirrors near the targets. High contrast is important for two primary reasons. The first is to ensure that little preplasma is formed at the laser facing side of the target prior to the arrival of the main pulse, which may adversely affect the absorption of laser coupling to the target ions, as was discussed in the previous section. The next reason is to ensure that no shocks are launched into the target. Amplified spontaneous emission (ASE) typically arrives nanoseconds before the main pulse, and given the small thickness of the targets used, could result in shock breakout, or target destruction before the main pulse has arrived. This work also utilized a larger focal spot diameter compared to previous experiments aimed at accessing the RPA regime. The focal spot diameter of ~4.1 microns FWHM was hypothesized to produce softer gradients transverse to the central focal spot which could prevent disruption of the RPA mechanism.

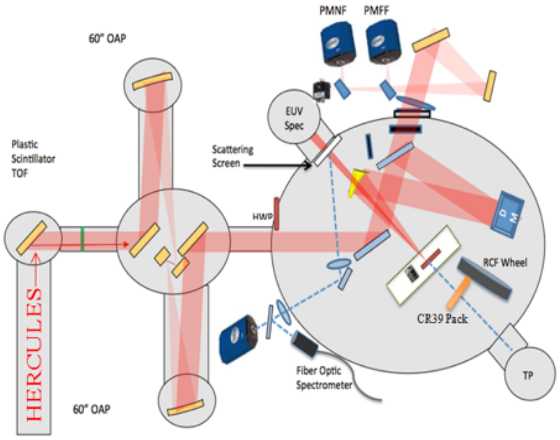

Figure 10. *The HERCULES experimental setup for ion beam acceleration.*

The experimental setup is shown in Fig. 10. The HERCULES laser is focused into the dual plasma mirror chamber, recollimated and sent into the experimental chamber. A deformable mirror just before the final focusing parabola served to correct aberrations in the laser wavefront. Several diagnostics were used to monitor the quality of the laser contrast and focal spot during each shot. Two spectrometers were used to monitor the reflected laser light from the laser-target interaction.

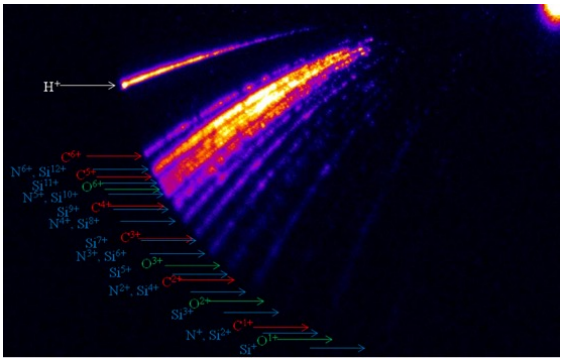

Figure 11. *Example signal from the Thomson parabola diagnostic. Each trace represents a charge-to-mass curve, with up to 15 distinguishable curves from H, C, Si, O, and N ions.*

The primary ion diagnostic was a Thomson parabola placed behind the target, which is capable of resolving tracks of ions with unique charge-to-mass (q/m) ratios, as well as their energies, an example of which is seen in Fig. 11. An optical CCD was coupled to a scintillator and microchannel plate (MCP) as the detector. In addition to this, CR-39 detectors were placed behind the target in order to identify the ion beam angular distribution.

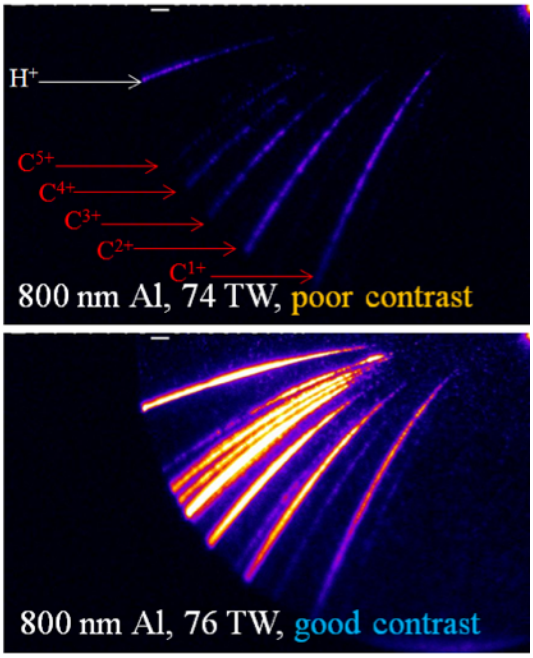

Figure 12. *Example signals from similar shots where the pulse contrast was poor or good. Enhanced contrast greatly improved ion acceleration.*

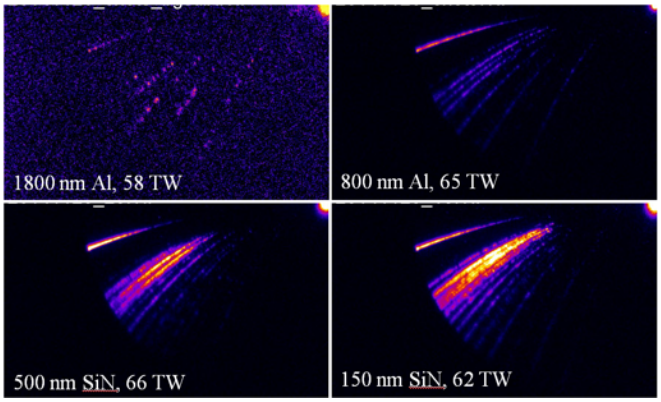

Figure 13. *Example signals from similar shots but differing target thickness. Thinner targets were seen to improve the acceleration of ion species other than protons.*

The targets were shot at normal laser incidence, and were either Si_3N_4 foils of thickness 8-500 nm, or metallic foils (Al, Ti, Cu) of thickness 200 nm or greater. Since no effort was made to remove hydrocarbon contaminants from the targets, H^+ and C^{1-6+} signals were present during all shots.

Two factors were identified to strongly influence the detection of ions other than H^+. These are the laser pulse contrast/quality, and the thickness of the foils used. For example, Fig. 12 shows a comparison between two shots of similar laser powers but good and poor contrast. When the laser contrast was poor, indicating that the plasma mirrors had been initiated early, few ion tracks were recorded compared to when the contrast was seen to be "good". Similarly, with good contrast, ion acceleration improved with decreasing target thickness, as seen in Fig. 13. The proton track was observed to saturate and remain approximately constant when the target thickness reached 200 nm. Below this thickness, the proton track remained, while the acceleration of heavier ion species increased until thicknesses of ~35-50 nm. The thinnest targets, 8 nm Si_3N_4 exhibited a decreased ability to produce ion beams with heavier elements.

While the enhancement of TNSA accelerated proton beams through the use of thinner (several micron thickness) targets has been observed, acceleration from sub-micron thick targets are typically affected by shock breakout due to the laser prepulse. This shock breakout destroys the sharp gradient at the rear surface, which is necessary for the TNSA mechanism to be effective. These observations show that the RPA mechanism is likely more effective as the target thickness decreases, in line with earlier theoretical work. Additionally, more recent theoretical work has shown the existence of an optimal target thickness for a fixed laser intensity, and is discussed in the following section.

III. Theoretical Exploration of Novel Targets for RPA Ion Beam Acceleration

a) *Optimization of Silicon target thickness to generate mono-energetic ion bunches*

Three set of simulations were carried out to obtain mono-energetic ion bunch and improve the peak energy value by two-dimensional Particle-in-Cell code EPOCH [24]. Each set of calculations were based on the HERCULES laser parameters, where 3.5 J energy was compressed into a 35 fs pulse with a peak intensity of 4.9×10^{20} W/cm^2.

In the first set of simulations, solid density silicon foil targets were examined. The target thickness was varied from 35 nm to 500 nm. It was found that 150 nm was the optimal thickness for the HERCULES laser pulse to generate mono-energetic ion beam, as seen in Fig. 14. While the 35 nm target thickness results in the acceleration of higher energy ions, there is a broad energy spread. The 500 nm

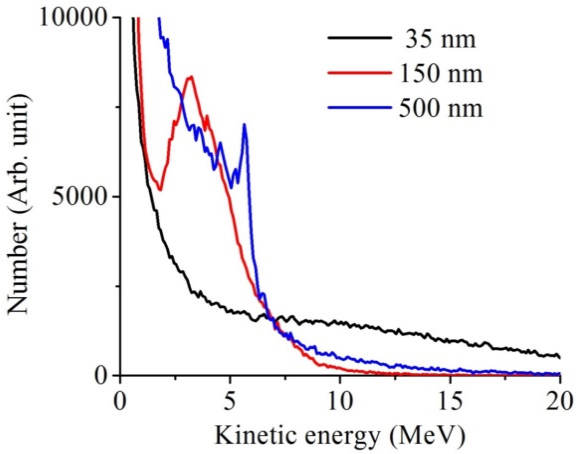

Figure 14. *Ion energy spectra generated from silicon targets of different thickness. The strongest/optimal ion bunching is observed for a thickness of 150 nm.*

target thickness results in similar ion energies as the 150 nm case, however, the bunching of Si ions for energies of 3-5 MeV is clearly improved in the 150 nm target thickness case.

We compared the density distributions for three different thickness to see the reason for optimal thickness. From the density distributions of 150 nm and 500 nm [seen in Fig. 15], one can see that the laser pulse was stopped by the high density plasma layer, meanwhile ions were accelerated out of the high density layer forming a high quality ion bunch. At the simulation time shown, 150 fs, the laser pulse is no longer on, meaning that there is no more interaction between the ion bunch and the laser pulse. The ion bunch was then stable to transport after being accelerated from the high density layer. The ions in the spectrum spike were located in front of the Hole-boring front, meaning that the mechanism to generate this ion beam was similar to Hole-boring Radiation Pressure Acceleration (HB-RPA) [25]. For thin target (35 nm), the interaction between the laser pulse and plasma was similar to Radiation Pressure Acceleration [26]. In the purely RPA situation, the plasma is pushed by the laser pulse through the interaction time, however the electric field inside the layer was not high enough to accelerate the ions off after the laser pulse has vanished, and no more electrons are forced in front. On the other hand, for thick target (500 nm), the thickness was enough to form a high density front with a large electric field inside it, from which ions can be accelerated off the high density layer. Since the target was thick enough, the interaction time was much longer than the thinner target (150 nm), and many ions were accelerated at lower laser intensity (the falling edge of the laser pulse), during which time the plasma density was lower and the electric field was smaller than during the main portion of the laser pulse. This results in many lower energy ions being accelerated out, which accounts for the increased number of low energy ions can be seen in the spectrum for the 500 nm simulation than that of 150 nm.

b) *The effect of pre-plasma scale-length on ion bunch energy*

In HB-RPA, the relation between ion bunch kinetic energy and plasma initial density can be expressed [2] as

$\varepsilon_i =$

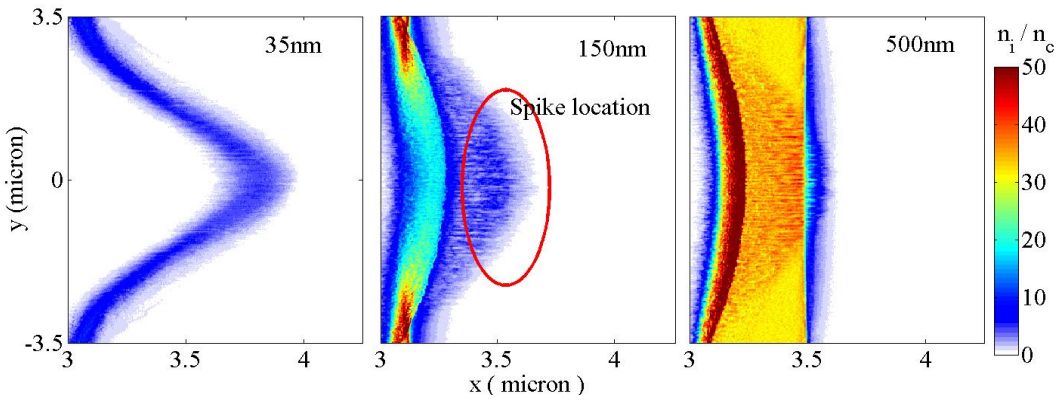

Figure 15. *The ion density distribution at 150 fs into the simulations for different target thicknesses. The strongest ion bunching is observed for the 150 nm target thickness.*

This suggests that higher kinetic energy can be obtained with lower plasma density. When an ultra-intense laser pulse irradiates on the target, the pre-pulse always arrives prior to the main pulse. The pre-pulse induces hydrodynamic expansion of the target at lower density. This reduced-density pre-plasma may be used to further enhance ion energy. Based on this consideration, we have simulated the effect of a low density pre-plasma on ion acceleration. In the simulations, the plasma density was set to linearly increase from a lower threshold density to solid density. Fig. 16 shows ion density distribution at the end of simulation, from which one can see that the ion bunch originates from the low density pre-plasma.

From the ion density distribution, we can find that the effective plasma density for acceleration was much lower than solid density as the acceleration happened in the pre-plasma regime. There was no interaction between the laser pulse and solid density part as the laser pulse was stopped by the hole-boring front. We have changed the pre-plasma scaling length to see the effects on ion energy. The pre-plasma size was varied between 0.4 μm to 2 μm. It was found that larger pre-plasma length gave higher ion energy as shown in Fig. 17. The ion energy for the 2.0 micron pre-plasma case was about 10 times higher than an ideal solid density target.

c) *Si and C nanofoam targets to further enhance ion bunch energy*

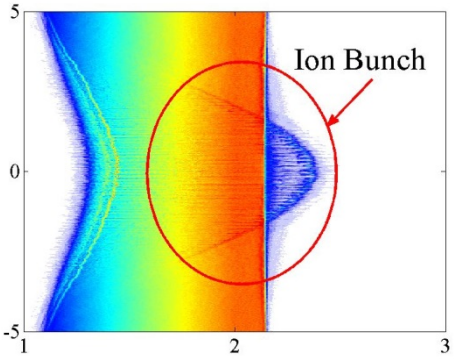

Figure 16. *The ion density distribution for a 1 micron scale-length pre-plasma in front of a solid target showing strong ion bunching.*

As discussed above, ion energy is related to plasma density, and lower density plasma can result in higher accelerated-ion energy. Silicon and carbon nanofoams [23] have been well developed in recent years, and are considered to be an effective method to reduce material density. We proposed silicon and carbon nanofoam targets to further reduce the plasma density. In these simulations, the plasma density was set to 5-10% of solid density. Fig. 18 shows the ion density distribution at the end of simulation, from which one can clearly see an ion bunch being accelerated from the target.

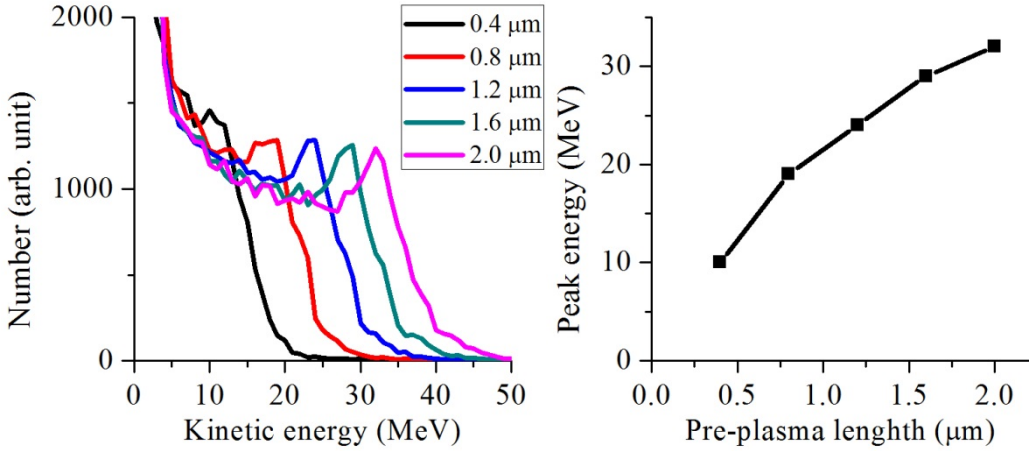

Figure 17. *(Left)Ion energy spectra generated from silicon targets with different pre-plasma lengths. (Right) The peak ion energy achieved as a function of pre-plasma scale length.*

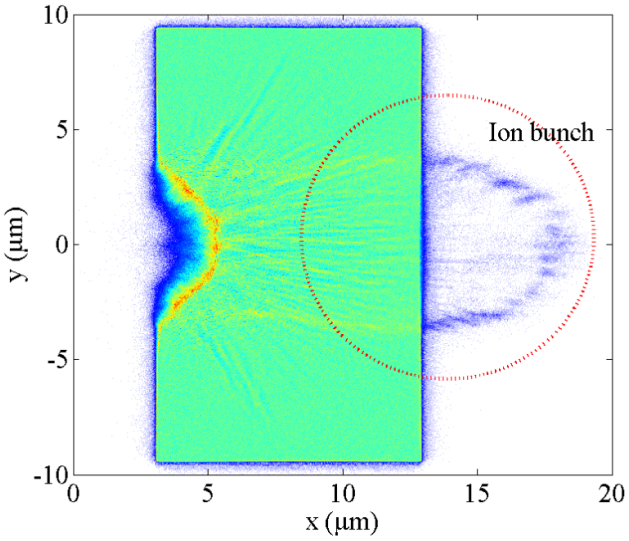

Figure 18. *Ion density distribution from a simulation using a silicon nanofoam target at 10% of solid density.*

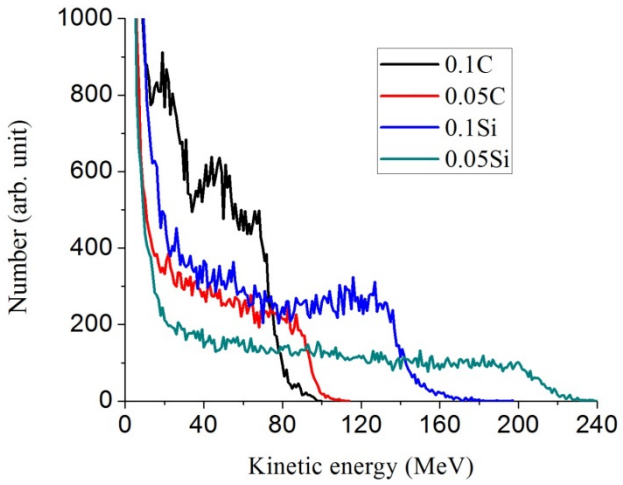

Figure 19. *Resulting ion energy spectra generated from simulations of nanofoam targets of different densities. The number left of the material indicates the fraction of solid density.*

These types of foams were simulated for various densities, and the resulting ion energy spectra for different densities are shown in Fig. 19. It was found that a silicon beam of peak energy around 120 MeV (carbon beam of peak energy around 50 MeV) can be generated with initial density of 10% solid density. Using nanofoams, the ion peak energy was near 30 times higher than the target of solid density target, and thus appears to be a promising avenue for increasing the energy of laser-accelerated ion beams.

In conclusion, several target designs have been examined numerically in order to find optimal parameters for maximizing the ion energies as well as enhancing the ion bunching. Using the HERCULES laser parameters, silicon ion acceleration was studied with 2D-PIC simulations. It is found that an optimal thickness exists at around 150 nm, which can generate mono-energetic ion beams. The effect of a pre-plasma formed on the laser-facing side of the target on ion beam acceleration was also examined. It was found that higher energy ions can be generated with a micron-scale pre-plasma, and larger pre-plasma length resulted in higher ion energy. To further reduce target and plasma density, we simulated C and Si nanofoam targets, which were also found to be an effective means of reaching higher ion energy. This theoretical work suggests multiple paths for increasing the ion beam energy while using the HERCULES laser system.

IV. Theoretical Optimization of Driver and Target Requirements for Heavy Ion Beam Production

The purpose of this work was to develop modeling and simulation capabilities for laser-target interactions to assist and guide experimental efforts dedicated to the program. Simulations will be used to compare model prediction with experimental data, guide experiments and develop theory for acceleration of heavy ions using short pulse lasers.

Numerical simulations were performed using the two-dimensional electromagnetic particle-in-cell (PIC) code developed at the Naval Research Laboratory (NRL) [28-30]. The code is relativistic, parallelized using MPI and can model laser-target interactions in two dimensions. The model uses an ionization model that dynamically updates the charge of each ion using a conventional Monte Carlo scheme [28]. The PIC code models the energy absorption from the laser pulse using a robust implicit algorithm to solve the Maxwell's equations, as well as the whole process of ionization and ion acceleration using computational particles. The PIC code is energy conserving, fast and extremely robust against numerical instabilities.

Input: (a) laser parameters: intensity, pulse duration and spot size; (b) target parameters:

configuration, material, dimensions.
Output: electron and ion beam parameters: energy spectra, flux, charge distribution and conversion efficiency.

There are no free or adjustable parameters. All laser and target parameters such as material, density, etc. use realistic values.

The work here consists of a parametric study, where extensive numerical simulations for Au targets are performed in a wide range of conditions by varying laser parameters (intensity, pulse duration and spot size) and target parameters (thickness, dimensions, flat vs. microdot, etc.). In addition to this a number of existing laser systems have been modeled (Hercules, Max-Born Institute (MBI), Astra-Gemini, Bella, Texas PW and Trident) in order to identify the most promising parameters for heavy ion acceleration. Studies on a more fundamental level were also performed in order to determine operational characteristics of different ion acceleration mechanisms, namely the Radiation Pressure Acceleration (RPA), Breakout Afterburner (BoA), and Target Normal Sheath Acceleration (TNSA) mechanisms.

a) *Identification of challenges associated with the acceleration of heavy ions*

There are several challenges for heavy ion acceleration compared to light ions. During the course of numerical investigation, we determined that unlike protons and light ions, the acceleration of heavy ions is much more challenging. There are numerous issues, accompanying the acceleration of heavy ions, and differences compared to ions from low-Z material:

- *Lower charge-to-mass ratio*. For heavy ions, *q/M* is twice lower compared to light ions [Fig. 20(a)], which has implications for the maximum ion energy the heavy ions can reach, as well as the competition between heavy ions and the ever-present contaminants on the target surface. The low *q/M* is disadvantageous for heavy ions and must be somehow overcome. This effect has already been seen experimentally for mid-Z ions.
- *Fewer ions available for acceleration*. Only those in the focal spot having large *q/M* can be efficiently accelerated.
- *Delayed acceleration*. Heavy ions can be accelerated only after the peak of the laser pulse [Fig. 20(b)]. This issue is more subtle and is unique for heavy ions. Ionization and acceleration are divided into two distinct phases separated in time, e.g. a phase of ionization and a phase of acceleration. During the first phase the ions must be ionized to very high charge states, a process that completes at the peak of the laser pulse. The second phase, acceleration, takes place during the pulse fall-off, shortening the time available for acceleration by a factor of two.
- *Plasma mirror effect*. Due to the large ion charge in the focal spot ($q \cong 50$), the electron density

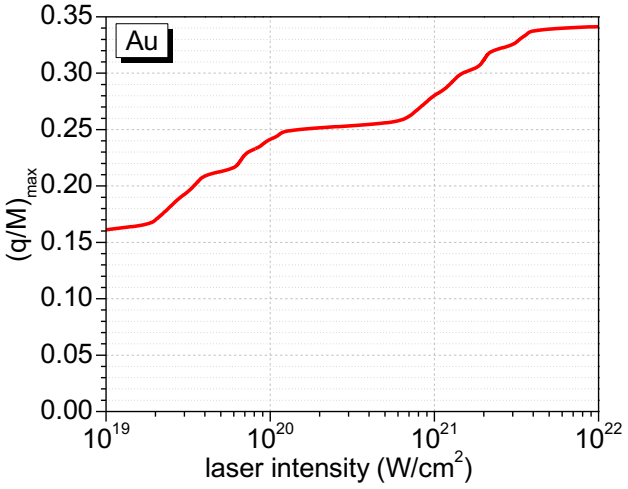

Figure 20a. *Maximum charge-to-mass ratio for gold ions vs. peak laser intensity.*

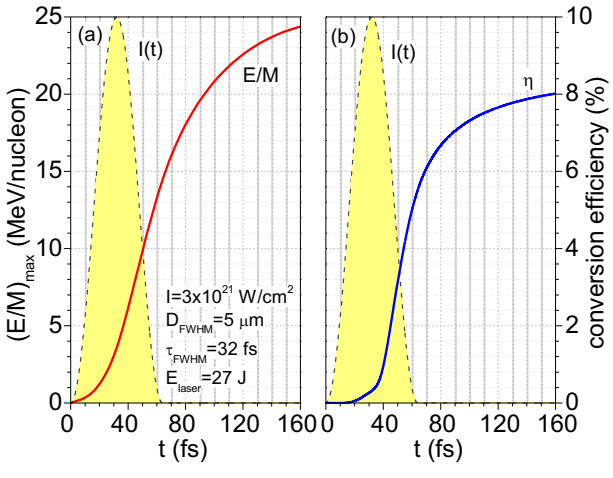

Figure 20b. *Maximum energy (a) and conversion efficiency into gold ions (b) vs. time. The yellow shaded is the laser pulse profile.*

becomes extremely high, $n_e / n_{crit} > 2000$ right at the moment the ion acceleration starts. The "plasma mirror" reflects most of the incoming laser radiation reducing the coupling of laser energy to plasma.

All those issues adversely affect the formation of heavy ion beams. Research at the fundamental level is being conducted to counter and overcome them.

b) *Parametric study of Au ion acceleration*

We performed very extensive parametric study of Au ion acceleration. The initial efforts were directed toward the Hercules laser. Numerical simulations were performed for laser parameters: 2 Joules energy, 40 fs duration, 1.5 μm spot size and intensity $2\times10^{21}\,W/cm^2$, interacting with a ultrathin (20-500 nm) gold foil.

i) Maximum ion energy versus foil thickness

First, we consider foil thickness variation for fixed laser parameters. Gold ion spectra are plotted in Fig. 21. For $L<100nm$ the maximum energy drops dramatically with foil thickness, which indicates transition from RPA to TNSA. For thickness For $L<100nm$ the foil is opaque to the electromagnetic field and the Au ions are accelerated via TNSA. The maximum gold ion energy versus laser intensity and ion spectra are plotted in Fig. 22 (a). The laser intensity varies from 10^{21} to $10^{22}\,W/cm^2$, corresponding to laser energy from 1 to 10 Joules. The foil thickness is 20 nm. The simulations showed that the calculated maximum energy scales as $E_{max} \sim I^{5/3}$, having power dependence exceeding that of TNSA. We surmise that the strong power dependence is a combination of two factors: more efficient transfer of laser energy to the bulk and gold ions charge increase with I increasing. As it was demonstrated in the previous figure, it is paramount to increase the laser intensity on target as much as possible for two reasons: (1) reach higher charge-to-mass ratios and (2) enter more efficient acceleration mechanism. This is usually achieved by reducing the laser focal spot size, but such reduction has an adverse effect on ion acceleration. In order to illustrate this point, the focal spot size was varied for a fixed laser intensity and pulse duration. The simulation results are plotted in Fig. 22(b). The most striking observation is that for spot size $D_{FWHM} < 5-8\,\mu m$ the maximum ion energy rapidly decreases with spot size, nearly canceling the gains made by intensity increase. Overall, there is little or no benefit to reduce the focal spot size below the optimal value of 5–8 μm.

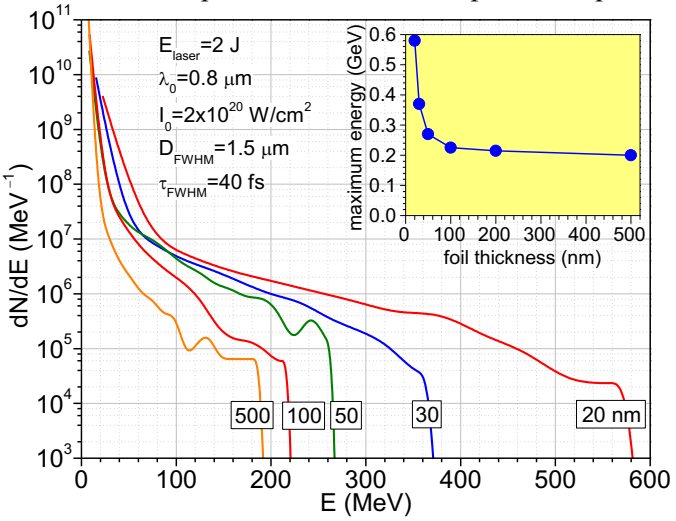

Figure 21. *Gold ion spectra from foils with thicknesses between 20 and 500 nm. Inset: maximum gold ion energy versus foil thickness. For L<100nm the ion acceleration mechanism is attributed to RPA For thickness L<100nm the Au ions are accelerated via TNSA.*

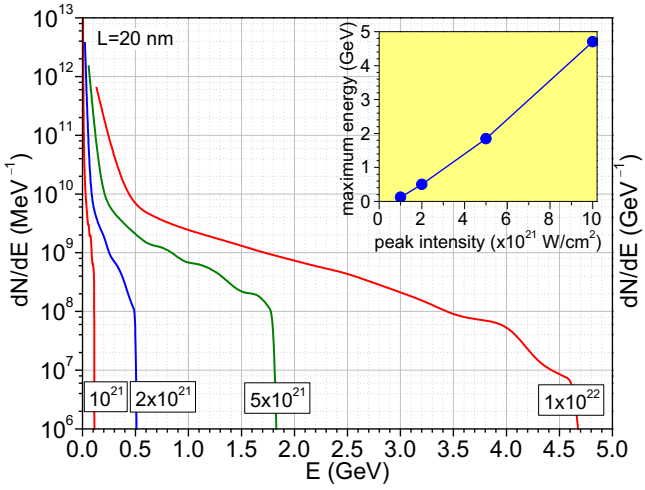

Figure 22a. *Gold ion spectra from a 20 nm foil for various laser intensities. Inset: maximum gold ion energy versus laser intensity.*

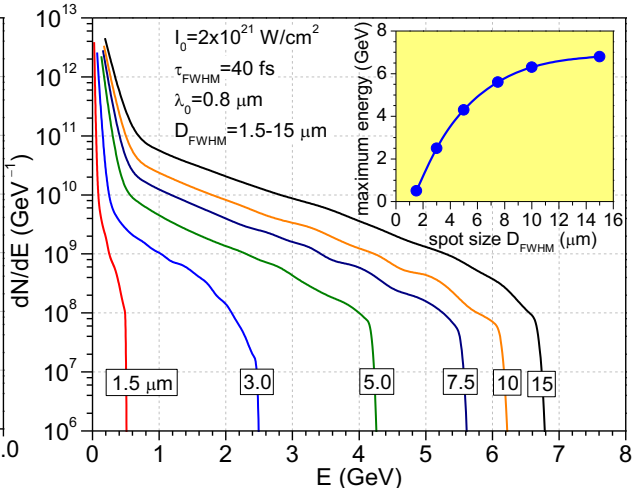

Figure 22b. *Gold ion spectra from a 20 nm foil for various laser focal spot sizes. Inset: maximum gold ion energy versus focal spot size.*

The parametric study established a parameter range suitable for heavy ion acceleration:

- Optimal foil thickness: ~20 nm
- Optimal spot size: 5–8 μm
- Optimal laser intensity: $>10^{20} W/cm^2$
- Optimal pulse duration: > 30 fs

Large intensity [Fig. 22(a)], spot size [Fig. 22(b)] and pulse duration >30 fs are required at the same time. The only possible solution is to use a laser with more energy (>10 J), for which all those conflicting requirements can be simultaneously satisfied without sacrificing [see Fig. 24]. In addition, the pico-and nano-second pre-pulse contrast must be very large ($>10^{10}$) in order to handle ultrathin (nm) targets.

c) *Ion beam properties*

The calculated charge distribution of gold ions is shown in Fig. 23. It is concentrated in the interval $15 < q < 45$ ($0.08 < q / M < 0.23$) and the maximum ion charge observed is $q_{max} = 51$. The average and maximum charge-to-mass ratios are and , respectively. Fig. 23 illustrates one of the challenges mentioned previously. The relatively low q/M combined with late energy transfer from electrons to gold ions is the main reason the maximum reduced ion energy to remain relatively low, ~3 *MeV/nucleon*.

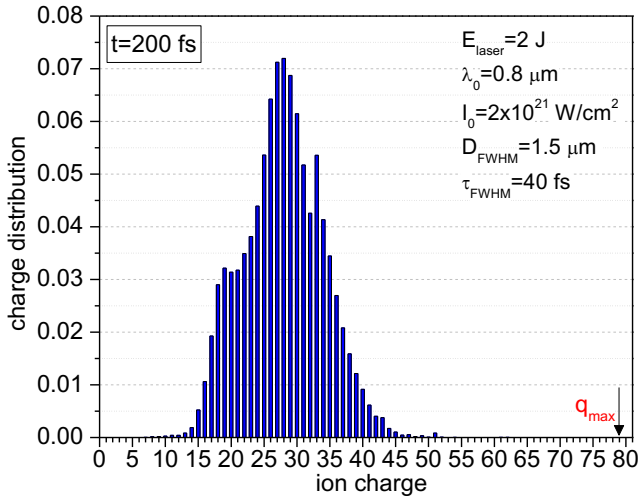

Figure 23. *Au ion charge distribution at the end of the simulations (200 fs).*

d) Ion beam properties for various laser systems

The predictive capabilities of the PIC code were used for evaluation of existing laser systems (Table 1). Simulations were performed and the Au ion beam parameters were compared.

Table 1. *Laser system parameters.*

Laser system	MBI	Astra	Bella	Texas PW	Trident
E (J)	1.4	6	27	50	85
I (10^{20} W/cm^2)	2.4	5	30	2.5	5
τ (fs)	32	48	30	180	600
D (μm)	4	4.7	5	10	5
λ (μm)	0.8	0.8	0.8	1	1
P (TW)	45	125	900	280	140

The maximum normalized ion energy E/M and Au ion flux $dN/d\Omega$ in the forward direction are plotted in Fig. 24. All laser systems except for MBI appear to be suitable for acceleration of gold ions. The predicted ion flux in Fig. 24(b) can be useful for planning experiments since it allows to assess the number of ions available for detection.

Based on the modeling efforts, the following conclusions can be made:

(a) modelling and simulation capabilities have been developed and matured enough to be used for comparison with experimental data, as well as a tool with predictive capabilities for guiding experiments.

(b) the laser and target parameter landscape for short pulse laser systems (30-50 fs) has been mapped. The most important finding is that numerous conflicting requirements are at place, which can be resolved by picking a laser with enough energy (>10 Joules on target)

(c) the predictive capabilities were used to evaluate existing laser systems.

V. Experimental demonstration of mono-energetic titanium ion beams

We performed an experiment of heavy ion acceleration on the Trident laser at the Los Alamos National Labs (LANL). This laser delivers 75 J during 650 fs focused to a 5 μm focal spot (FWHM) for an intensity of ~7×10^{20} W/cm^2 with an intensity contrast close to 10^{-12}. The interaction of the Trident laser with sub-micron thick targets allowed acceleration of heavy ions to high energies. Before recording the ion spectra, we used the iWasp diagnostic to find the angular distribution of the ions. The iWasp diagnostic was placed at the back of the target. It consists of a slit and a magnet; the magnet deflects the ions depending of their mass and energy and the slit allows measurement of the angular distribution of ions across a 45° span. Contrary to the results in the literature, the ion beam peaked away from the rear target normal. Two Thomson Parabolas (TPs) were placed at different angles: 0° and 11°

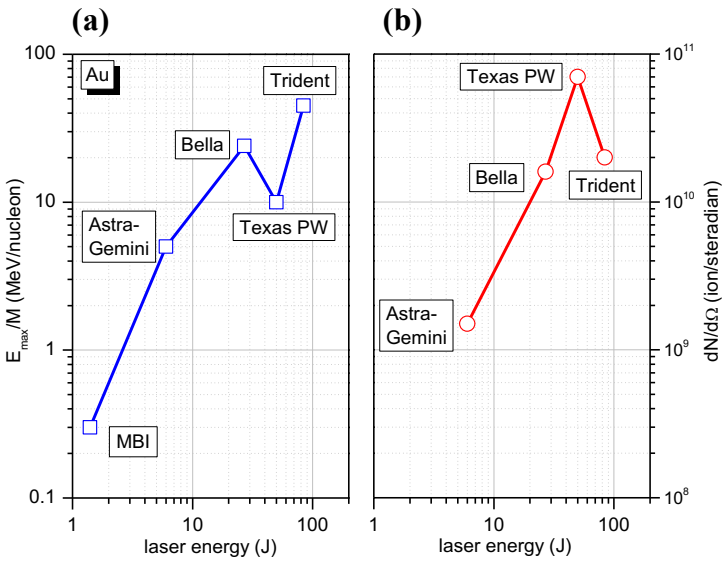

Figure 24. (a) *Maximum normalized ion energy (b) and Au ion flux for various laser systems.*

from the target normal. The TP splits the different ions species and their energies allowing the measurement of spectra for the different ionization states on an Image Plate (IP). The experimental setup is shown in Fig. 25. Targets of various materials (Ti, Ge and Co) and thicknesses (60 to 140 nm) were used, however, our focus was on acceleration of Ti ions.The Trident laser delivers 75 J in 650 fs and is focused in our experiment at normal incidence on titanium

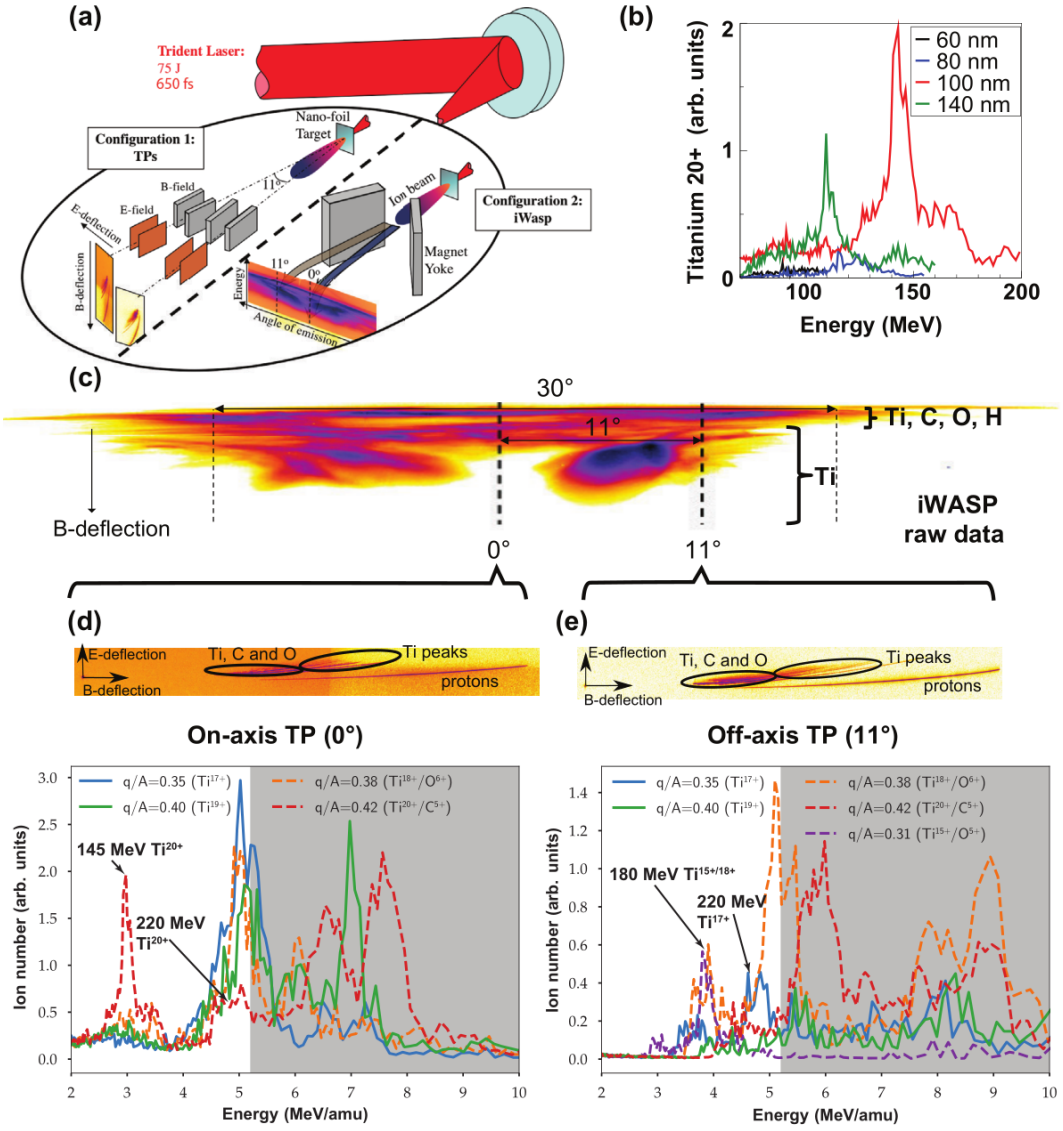

Figure 25. *Summary of the experimental results using the 120 TW Trident laser focused to peak intensities of 6×10^{20} W/cm^2 onto titanium foils of thicknesses from 60 to 140 nm. (a) Schematic of experiment setup. Two diagnostic configurations were used: Configuration 1) two Thompson Parabolas (TP) located at respectively 0° and 11° from target normal, measuring the energy spectra of collected ions depending on their q/A ratio. Configuration 2) an ion wide-angle magnetic spectrometer (iWASP) giving angularly resolved ion energy spectra. Both instruments used image plate (IP) as detectors. (b) Ti^{20+} spectra obtained for the different titanium target thicknesses. An optimum both in terms of accelerated energy and ion number is obtained for the 100 nm thickness. (c) Raw iWASP result showing concentration of titanium ions close to 11°. Ion spectra in energy-to-mass ratio (MeV/amu) corresponding to various ion species at target normal (d) and at 11° from target normal (e), for 100 nm target thickness. Quasi-monoenergetic peaks of ions are observed both on-axis and o-axis. A clear predominance of Ti^{20+} ions are observed on-axis (peaking at 145 ± 10 MeV) while multiple ionization states are observed o-axis (Ti^{15+} and Ti^{18+}) peaking at 180 MeV. The gray shaded region starting at 5.3 MeV/amu corresponds to data where traces having q/A difference of <0.2 have overlapping signal.*

nano-foils of different thicknesses ranging from 60 to 140 nm, reaching a peak intensity on-target of 6×10^{20} W/cm^2 with a 50 ps intensity contrast of 10^{-9}. It is worth mentioning that the laser contrast $< 10^{-9}$ was good enough to preserve target integrity prior to the main pulse interaction and is undoubtedly crucial for efficient heavy-ion acceleration from ultra-thin targets. We measured the accelerated heavy-ion angular distribution and energy spectrum using a wide-angle magnetic spectrometer (iWASP) and a set of two Thomson Parabolas (TP) located at 0° and 11° from target normal. The first configuration with the wide-angle spectrometer allowed us to determine the preferred angles to be explored. The setup for the two configurations is shown in Fig. 25(a). In Fig. 25(c-e), we show the iWASP result obtained for 100 nm thickness and the resulting spectra on TP at 0° and 11° from target normal. The iWASP signal clearly shows the emission of ions both on- and off- target axis. The off-axis population shows a peak around 11°, where we accordingly positioned our second TP. Moreover, we did not observe any caustic "filaments" in the angular ion distribution measured by the iWASP, which may have caused unreliable single-point measurements with TPs, which have a very small collecting angle. In Fig. 25(d)(e), we present the ions energy spectra in energy per nucleon (MeV/amu) for TP traces corresponding to different ratios of ion charge q to ion atomic mass A , as shown in the raw TP data on top of each figure for on-axis and off-axis respectively, with a focus on high-yield titanium ions accelerated from the target bulk. The acceleration of protons and other contaminants (C, O) are not discussed here, as it results from already well-studied mechanisms in literature both for TNSA and RIT/BOA mechanisms. However, the part of the ion spectra with an energy per nucleon greater than 5.3 Mev/amu has to be regarded with caution since nearby traces separated by a difference in q/A of 0.02 start to overlap. Therefore, nearby contaminant traces can contribute to the extracted signal, and as a result it is difficult to distinguish both populations on the image plate (IP) detector. The transition to the area of the spectrum where impurity traces are overlapping, at 5.3 MeV/amu, is highlighted in gray on the figures. Here, we will discuss the peaks pointed by the arrows in Fig. 25(d)(e). Indeed, they correspond to peaks which have been identified further in simulations and belongs to a part of the spectrum where there is no doubt about their nature.

The unfolded on-axis spectra [Fig. 25(d)] reveals quasi-monoenergetic titanium ions with a clear predominance of Ti^{20+} ions, peaking strongly at 145 MeV with a less pronounced peak at 220 MeV. Other ionization states identified from the other traces barely emerge from the noise. The off-axis lines [Fig. 25(e)] correspond to multiple titanium ionization states (from 15+ to 20+) with a peak at a slightly higher energy of 180 MeV for Ti^{15+} and Ti^{18+} and at 220 MeV for Ti^{17+} .The different behaviors observed between the ionization states and energy of on-axis and off-axis ions are remarkable and indicate that the electromagnetic fields experienced by the two ion populations are effectively different. In particular, the unique mono-energetic spike of Ti^{20+} observed on-axis suggests that all the ions are strongly ionized by the optical field of the laser to Ti^{20+}. Surprisingly, for off-axis ions, despite having a slightly higher energy, the ionization levels and yields are lower. To the extent that the ionizing and accelerating fields are the same, this seems at first glance contradictory. We will show later based on numerical simulations that both on- and off-axis ions experience similar fields, but the off-axis ions are effectively accelerated for longer time and therefore achieve higher kinetic energies. In Fig. 25(b), we present on-axis acceleration of Ti^{20+} ions for different target thicknesses used in the experiment (60, 80, 100 and 140 nm). It appears that the energy and number of the accelerated Ti^{20+} ions are significantly higher for the 100 nm thickness with respect to other thicknesses. Indeed, we observed very poor acceleration of titanium ions in our experimental detection range (100 MeV to 200 MeV) for both 60 and 80 nm thicknesses, although a clear quasi-monoenergetic peak similar to that of 100 nm is still observed for 140 nm at 110 MeV, with about half number of ions. Further, we focus on the optimum 100 nm thick target for the analysis of the acceleration processes.

VI. Simulations of mono-energetic and low-divergence titanium ion beams

We performed 2D particle-in-cell (PIC) simulations with fully-relativistic EPOCH code to model the laser-target interaction and ion acceleration in the experiments. The simulation results of the Ti^{20+} spectra are shown in Fig. 26(a)(b). The quasi-mono-energetic peaks circled by red lines agree well with the experimental results (near 145 MeV along on-axis direction and 225 MeV along off-axis direction). We found that the laser pulse breaks through the target during the interaction due to the relativistically

induced transparency (RIT). The ionization states of the target ions when the target is broken through are shown in Fig. 26(c). The on-axis Titanium ions located in the laser field are all ionized to Ti^{20+} due to the strong laser field, but the off-axis ions only reach Ti^{12+} due to the weak sheath field on the sides (off-axis). This qualitatively explains the experiments, which show the dominance of Ti^{20+} in the ions detected along the on-axis direction, but mixed ionization states along the off-axis direction.

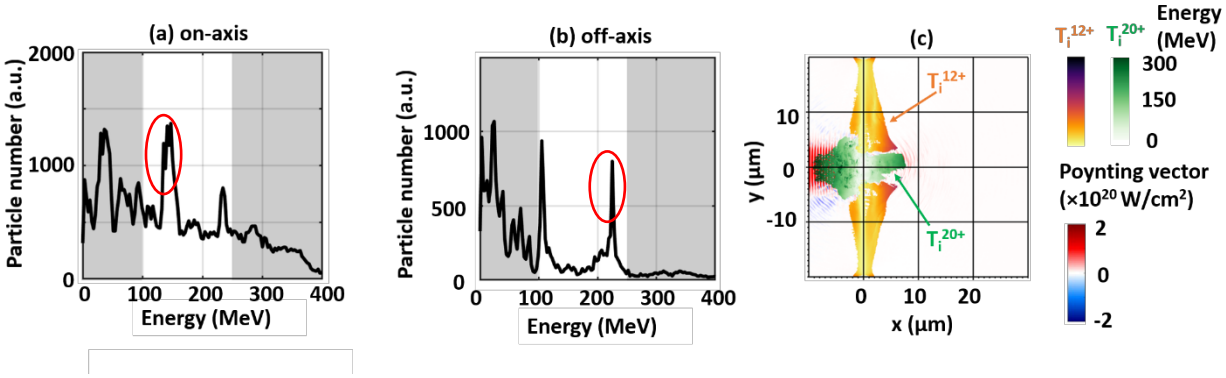

Figure 26. *The energy spectra of the Ti^{20+} ions along (a) on-axis and (d) off-axis directions. The red circles mark the quasi-mono-energetic peaks that agree with the experiments. The ions on the marked peaks are tracked to study the acceleration mechanism (c) The ionization states of titanium ions when the laser breaks through the target with thickness of 100 nm.*

The energy and angle histories of these Ti^{20+} ions on the peaks [circled in Fig. 26(a) and (b)] were tracked through the whole simulations. The analysis in showed that the ions are accelerated in two stages. Before the onset of RIT, the tracked ions are accelerated by the sheath field of target normal sheath acceleration (TNSA) mechanism. The acceleration in this stage is strong, and corresponds to the steep curves in Fig. 27(a)(c) before time t~-150 fs. After the onset of RIT, these ions were accelerated slowly by the self-generated electric field, which corresponds to the relatively less steep curves in Fig. 27(a)(c) after time t ~ -150 fs until the end of the simulation.

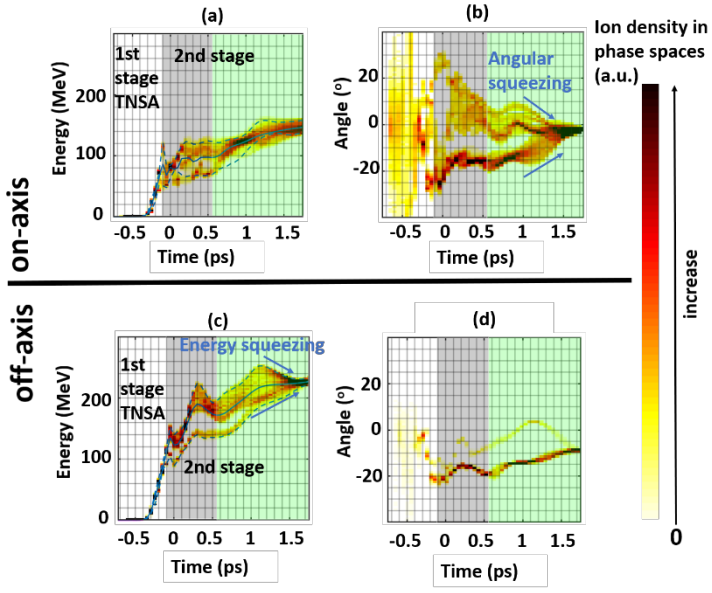

Figure 27. *The distributions of the tracked ions on the (a-b) on-(145 MeV) and (c-d) off-axis (225 MeV) peaks in Fig. 26(a)(b) in two phase spaces: (a)(c) time and energy and (b)(d) time and angle. The solid lines in (a)(c) are the averaged energy among all the tracked on- and off-axis ions. The dashed lines are from individual ions which are chosen to approximately represent the energy spread limits of all the tracked ions.*

The on- and off-axis peaks had different formation mechanisms. By comparing Fig. 27(a)(b) and (c)(d), we found that the on-axis peak was formed through angular squeezing, while the off-axis peak was formed by squeezing in energy space. This difference is caused by the different self-generated electric fields in the on- and off-axis region.

This combination of the two acceleration mechanisms, together with the peak formation processes, have never been studied in previous research. They significantly shed light on the mid-Z ion acceleration physics in this RIT-enhanced acceleration regime. Based on these simulations and the corresponding experimental results, we have drafted a manuscript which is being reviewed by the co-authors. This

manuscript has been submitted to *Nature communications*.

VII. Ionization injection of highly-charged copper ions for laser driven acceleration from ultra-thin foils

This piece of work is about an ion acceleration process in which the ionization occurs simultaneously with acceleration. Using particle-in-cell simulations, we have examined acceleration and simultaneous field ionization of copper ions in ultra-thin targets (20 - 150 nm thick) irradiated by a laser pulse with intensity 1×10^{21} W/cm^2. At this intensity, the laser pulse drives strong electric fields at the rear side of the target that can ionize Cu to charge states with valence L-shell or full K-shell. The highly-charged ions are produced only in a very localized region due to a significant gap between the M- and L-shells' ionization potentials and can be accelerated by strong, forward-directed sections of the field. Such an "ionization injection" leads to well-pronounced bunches of energetic, highly-charged ions.

The picture of the ionization injection concept is demonstrated in Fig. 28(a)(b), which shows the electric field E_x and the scattered plot of Cu^{25+} during the laser-target interaction. We can see that the E_x field is much stronger near the laser axis [Fig. 28(a)]. And only in the region with strong E_x, the ionization to 25+ can only be reached, as shown in Fig. 28(b). This mechanism causes ionization to high charge states only in strong E_x fields, forming ionization injection process. Quasi-mono-energetic ions with high charge states (>20) can be generated through this process, as shown in Fig. 29. The energy spectra are exponential for low charge states (19+), but for higher states (>20), the features of quasi-mono-energetic peaks can be observed.

Considering that the laser-driven mid-Z ions have not been well studied before, this ionization injection mechanism will have wide impact in the field of heavy ion acceleration. In our recent experiments on Phelix laser facility, this mechanism is inferred from the experimental results, and we will perform new simulations to study this mechanism in our proposed allocation on Comet.

VIII. Validation of experimental data and predictive capability for various laser parameters

We used modeling and simulations to benchmark experimental data and design experiments for specific laser conditions. The main goal of the theoretical work was to understand the fundamental physics and mechanisms of ion acceleration from mid- to high-Z materials, as well as support and interpret experimental data. In particular, we aimed to i) develop concepts and understanding of the

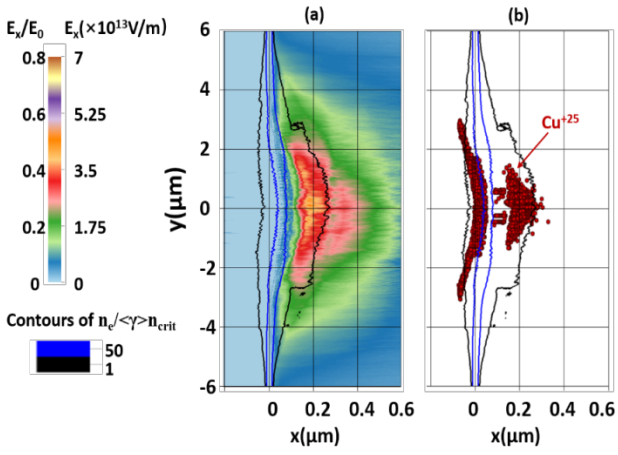

Figure 28. *Snapshots of the longitudinal electric field (E_x > 0 only) and Cu^{+25} ions for a target whose initial thickness was 20 nm. The black and blue curves are the contours of the electron density averaged over one laser period. The field is normalized to $E_0=8.6\times10^{13}$ V/m, which is the peak laser electric field at the focal spot when the target is not present.*

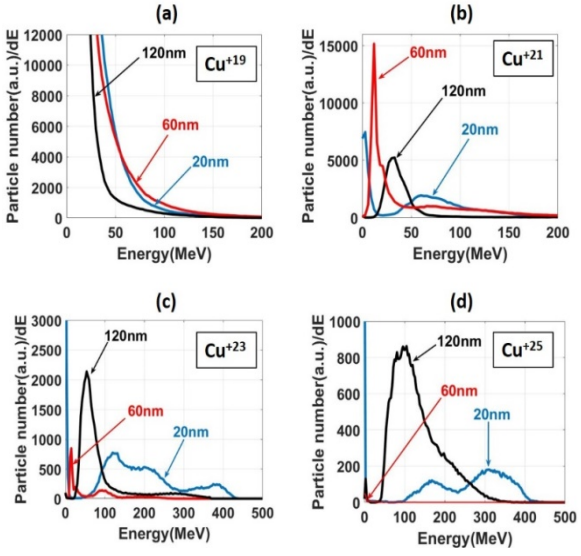

Figure 29. *Energy spectra of Cu^{+19}, Cu^{+21}, Cu^{+23} and Cu^{+25} ions for target thicknesses of 20, 60 and 120 nm at the end of the simulation.*

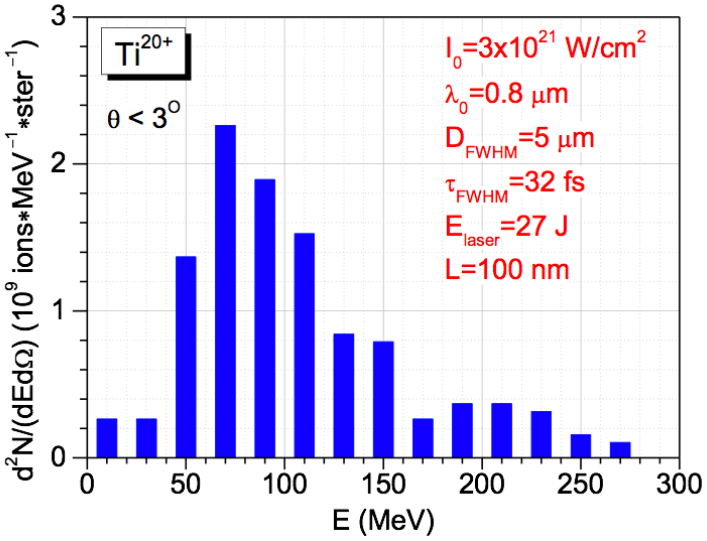

*Figure 30: Ti ion spectra from a curved foil with thickness 100 nm on the **Bella** laser. Ions are collected only in the forward direction within 3 degrees from the target normal with kinetic energy >0.5 MeV/nucleon.*

underlying physics of mono-energetic ion generation, and ii) model the generation of mono-energetic ions on existing laser systems in the US: Hercules, Bella, Texas Petawatt Laser and Trident lasers.

We used two different approaches and codes. First, we present results from the EPOCH particle-in-cell (PIC) code at UCSD that we used to benchmark with experimental data obtained on the Trident laser. Then, we present results from the PIC code used at the Naval Research Laboratory, which include a novel idea for generation of mono-energetic ions and supporting numerical simulations.

We performed a parametric study of Ti ion acceleration from curved targets using different laser systems (Trident, TPW, Bella). The initial efforts were directed toward targets with thickness 100-300 nm, comparable to those in the LANL experiment. In all simulations "clean" pulses were used. Additional simulations with finite contrast, e.g. flat targets with pre-plasma, did not produce mono-energetic ions. As a demonstration of the concept, numerical simulations are shown in Fig. 30 for the Bella laser with laser parameters: 27 Joules energy, 32 fs duration, 5 μm spot size and peak intensity $3\text{x}10^{21}$ W/cm^2. The foil thickness was 100 nm.

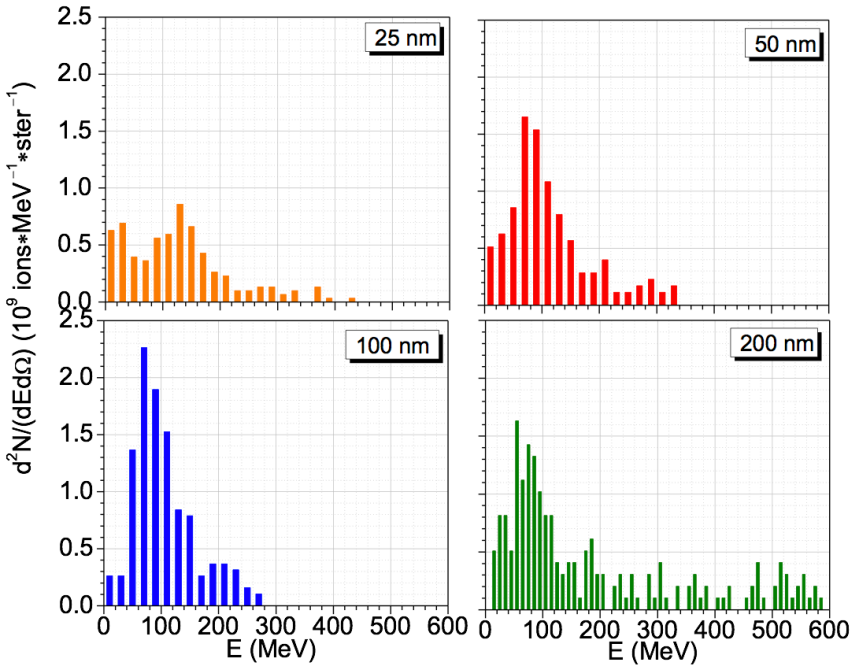

*Figure 31. Ti^{20+} ion spectra from a curved foil with thickness 25-200 nm on the simulated **Bella** laser. Ions are collected only in the forward direction within 3 degrees from the target normal with kinetic energy >0.5 MeV/nucleon.*

A foil thickness scan indicates that there is an optimum thickness of about 100 nm [see Fig. 31].

We surmise that the optimum foil thickness occurs because the onset of acceleration must be timed to coincide with the peak of the pulse. The hole-boring length for Bella $\ell_{HB} = \text{v}_{HB}\tau_{FWHM}/2$ is about 80 nm, where $\frac{\text{v}_{HB}}{c} = \sqrt{\frac{I}{m_i n_i c^3}}$ is the normalized hole-boring velocity, m_i and n_i are the ion mass and density and c is the speed of light. This estimate is in good agreement with the optimum foil thickness.

Before carrying out simulations to benchmark our Ti experimental data, we made simulations with a 200 nm Al

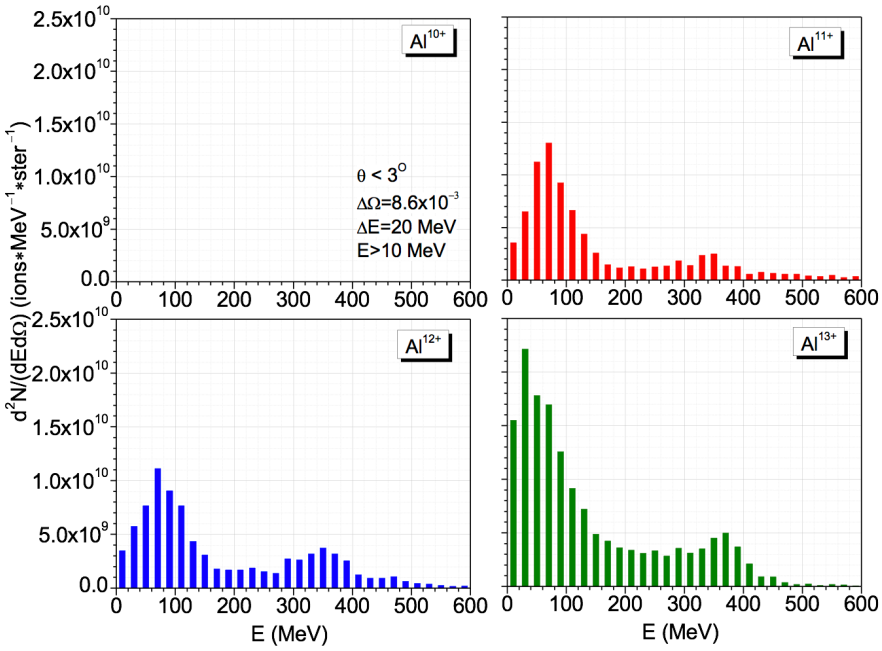

***Figure 32**: Al ion spectra from a curved foil with thickness 200 nm on the simulated **Trident** laser. Ions are collected only in the forward direction within 3 degrees from the target normal with E>0.5 MeV/nucleon. $I=4x10^{20}$ W/cm^2, λ=1 mm, D_{FWHM}=5 μm, τ_{FWHM}=650 fs, ε_{laser}=74 J.*

have the mono-energetic features seen in curved foils.

foil shown in Fig. 32. The simulations were motivated by the observation of mono-energetic Al ions on the Trident laser at similar conditions, mentioned earlier, therefore we attempted to reproduce them. Mono-energetic structures are indeed seen for Al with charges 11 and 12 [Fig. 32]. The simulation results support the data from these experiments, which were published in Nature Communications and provide a reference for simulations.

Analogous simulations were performed for a flat foil. The results are shown in Fig. 33. The ion spectra are exponential and do not

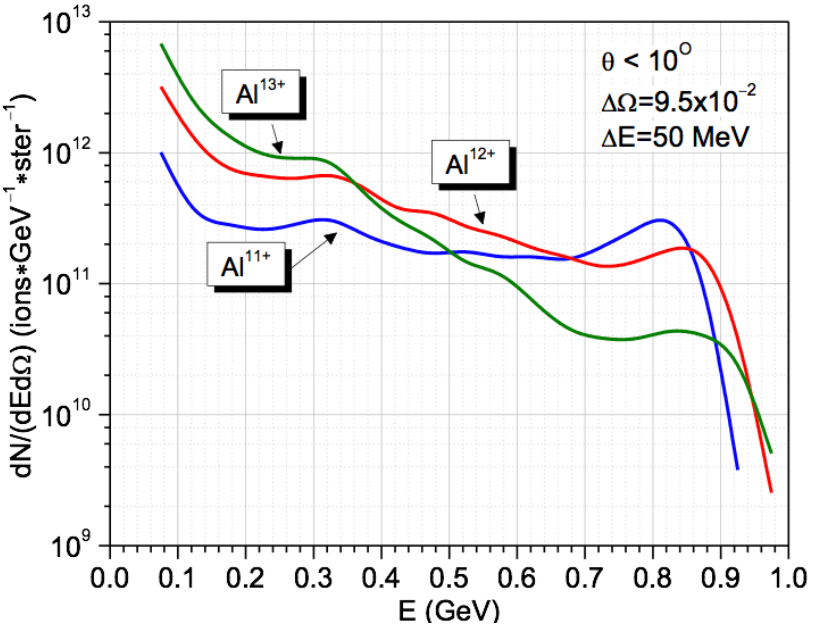

***Figure 33**: Al ion spectra from a flat foil with thickness 200 nm on the simulated **Trident** laser. The laser parameters are the same as in Fig. 32.*

We have a scheduled experiment on the Texas Petawatt laser at the University of Texas Austin. Simulations also show mono-energetic features for Ti^{20+} [Fig. 34].

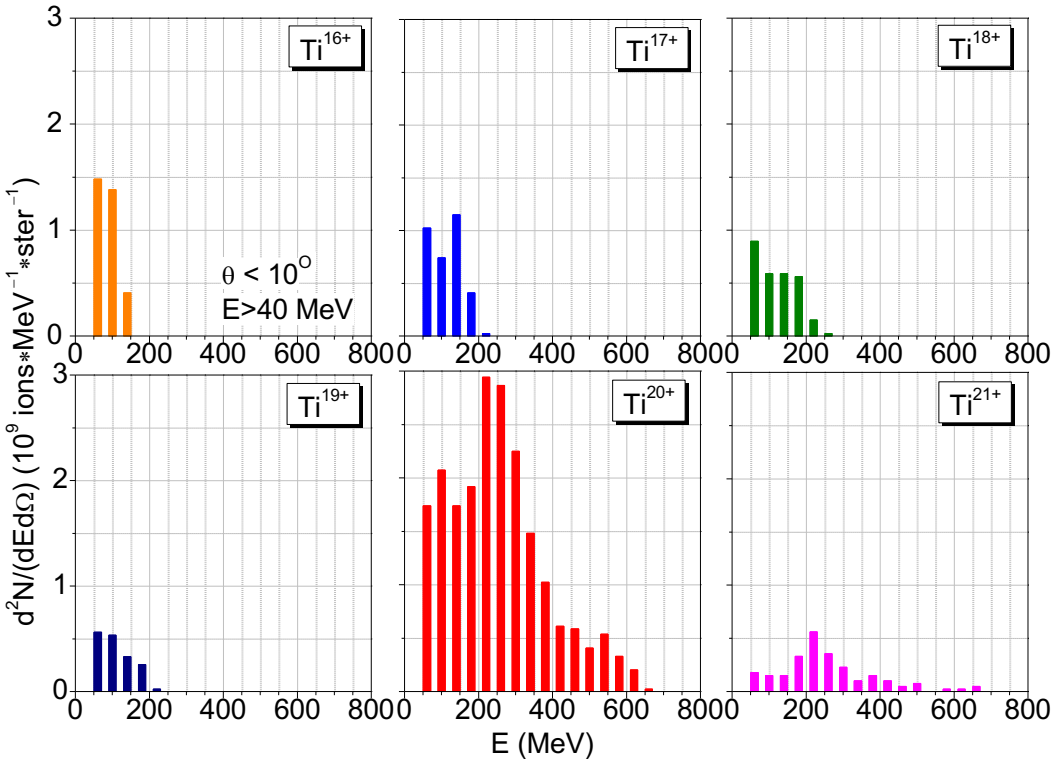

Figure 34. *Ti ion spectra from a curved foil with thickness 150 nm on the simulated **TPW** laser. Ions are collected only in the forward direction within 10 degree from the target normal with E>0.5 MeV/nucleon. I=2.5x10^{20} W/cm^2, λ=1 mm, D_{FWHM}=10 μm, τ_{FWHM}=180 fs, ε_{laser}=50 J.*

Based on the modeling efforts, the following conclusions can be made:

1. Curved foils are the key to producing monoenergetic ions.
2. Trident, Texas Petawatt and Bella lasers show monoenergetic-like structures from curved foils with thickness of about 150 nm. These structures do not appear for flat foils.
3. Target thickness scan indicate that there is an optimum thickness. For Bella it is about 100 nm. We surmise that the onset of acceleration should be timed to coincide with the peak of the pulse (transparency for Trident, hole-boring for Bella).

4. Publications

- **Generation of high-energy mono-energetic heavy ion beams by radiation pressure acceleration of ultra intense laser pulses**
  D. Wu, B. Qiao, C. McGuffey, X. T. He, and F. N. Beg
  Physics of Plasmas 21, 123118 (2014).
- **Proton acceleration from high-contrast short pulse lasers interacting with sub-micron thin foils**
  G. M. Petrov, C. McGuffey, A. G. R. Thomas, K. Krushelnick and F. N. Beg
  J. Applied Physics **119**, 053302 (2016).
- **Generation of heavy ion beams using femtosecond laser pulses in the Target Normal Sheath Acceleration and Radiation Pressure Acceleration regimes**
  G. M. Petrov, C. McGuffey, A. G. R. Thomas, K. Krushelnick, and F. N. Beg
  Physics of Plasmas, **23**, 063108 (2016).
- **Acceleration of high charge state target ions in high-intensity laser interaction with sub-micron**

targets
C. McGuffey, A. Raymond, T. Batson, R. Hua, G.M. Petrov, J. Kim, C.M. Krauland, A. Maksimchuk, A.G.R. Thomas, V. Yanovsky, K. Krushelnick and F.N. Beg
New Journal of Physics **18**, 113032 (2016).

- **High Repetition-Rate Neutron Generation by Several-mJ, 35 fs pulses interacting with Free-Flowing D_2O**.
  J. Hah, G. M. Petrov, J. A. Nees, Z-H. He, M. D. Hammig, K. Krushelnick, and A. G. R. Thomas
  Applied Physics Letters **109**, 144102 (2016).
- **Target Surface Area Effects on Hot Electron Dynamics from High Intensity Laser Plasma Interactions**
  C Zulick, A Raymond, A McKelvey, V Chvykov, A. Maksimchuk, A G R Thomas, L Willingale, V Yanovsky, and K Krushelnick
  New J. Physics **18**, 063020 (2016).
- **Heavy ion acceleration in the Radiation Pressure Acceleration and Breakout Afterburner regimes,**
  G. M. Petrov, C. McGuffey, A. G. R. Thomas, K. Krushelnick, and F. N. Beg
  Plasma Phys. Contr. Fusion **59**, 075003 (2017).
- **Ionization injection of highly-charged copper ions for laser driven acceleration from ultra-thin foils**
  Jun Li, Alexey V. Arefiev, Stepan S. Bulanov, Mathieu Bailly-Grandvaux, George M. Petrov, Christopher McGuffey, and Farhat N. Beg
  Nature Scientific Reports **9**, 666 (2018).
- **Optimization of laser-nanowire target interaction to increase the proton acceleration Efficiency**
  M. Dozieres, G. M. Petrov, P. Forestier-Colleoni, P. Campbell, K. Krushelnick, A. Maksimchuk, J. J. Rocca, C. McGuffey, and F. N. Beg
  Plasma Physics and Controlled Fusion (under review)
- **Laser acceleration of mono-energetic and low-divergence titanium ion beams**
  J. Li, P. Forestier-Colleoni,1 M. Bailly-Grandvaux, C. McGuffey, A.V. Arefiev, S.S. Bulanov, D.C. Gauthier, J. Peebles, C. Krauland, A. Hussein, T. Batson, J.C. Fernandez, S.Palayinappan, R.P. Johnson, G. Petrov, and F.N. Beg
  Nature Communications (under review)

REFERENCES

[1] G. N. Flerov and V. S. Barashenkov, Sov. Phys. Usp. 17, 783 (1975)
[2] K. W. D. Ledingham, P. McKenna, R. P. Singhal, Science 300, 1107 (2003)
[3] M. Baba, Nuclear Eng. Tech. 38, 319 (2006)
[4] P. McKenna, K. W. D. Ledingham, J. M. Yang, L. Robson, T. McCanny, S. Shimizu, R. J. Clarke, D. Neely, K. Spohr, R. Chapman, R. P. Singhal, K. Krushelnick, M. S. Wei, and P. A. Norreys, Phys. Rev. E 70, 036405 (2004)
[5] D. Habs, P. G. Thirolf, M. Gross, K. Allinger, J. Bin, A. Henig, D. Kiefer, W. Ma, J. Schreiber, Appl. Phys. B 103, 471 (2011)
[6] D. Kramer, Phys. Today 68, 24 (2015)
[7] S. C. Wilks, A. B. Langdon, T. E. Cowan, M. Roth, M. Singh, S. Hatchett, M. H. Key, D. Pennington, A. MacKinnon, and R. A. Snavely, Phys. Plasmas 8, 542 (2001)
[8] L. Robson, P. T. Simpson, R. J. Clarke, K. W. D. Ledingham, F. Lindau, O. Lundh, T. McCanny, P. Mora, D. Neely, C.-G. Wahlström, M. Zepf and P. McKenna, Nature Physics 3, 58-62 (2007)
[9] R. A. Snavely, M. H. Key, S. P. Hatchett, I. E. Cowan, M. Roth, T. W. Phillips, M. A. Stoyer, E. A. Henry, T. C. Sangster, M. S. Singh, S. C. Wilks, A. MacKinnon, A. Offenberger, D. M. Pennington, K. Yasuike, A. B. Langdon, B. F. Lasinski, J. Johnson, M. D. Perry, and E. M. Campbell, Phys. Rev. Lett. **85**, 2945 (2000).

[10] S. P. Hatchett, C. G. Brown, T. E. Cowan, E. a. Henry, J. S. Johnson, M. H. Key, J. a. Koch, a. B. Langdon, B. F. Lasinski, R. W. Lee, A. J. Mackinnon, D. M. Pennington, M. D. Perry, T. W. Phillips, M. Roth, T. C. Sangster, M. S. Singh, R. a. Snavely, M. a. Stoyer, S. C. Wilks, and K. Yasuike, Phys. Plasmas **7**, 2076 (2000).
[11] A. Macchi, S. Veghini, and F. Pegoraro, Phys. Rev. Lett. **103**, 085003 (2009).
[12] B. Qiao, M. Zepf, M. Borghesi and M. Geissler, Phys. Rev. Lett. 102, 145002 (2009).
[13] B. Qiao, M. Zepf, M. Borghesi, B. Dromey, M. Geissler, A. Karmakar, and P. Gibbon, Phys. Rev. Lett. **105**, 155002 (2010).
[14] L. O. Silva, M. Marti, J. R. Davies, R. A. Fonseca, C. Ren, F. S. Tsung and W. B. Mori, Phys. Rev. Lett. 92, 015002 (2004).
[15] C. McGuffey, A. Raymond, T. Batson, R. Hua, G. M. Petrov, J. Kim, C. M. Krauland, A. Maksimchuk, A. G. R. Thomas, V. Yanovsky, K. Krushelnick, and F. N. Beg, New J. Phys. **18**, 113032 (2016).
[16] L. Yin, B. J. Albright, B. M. Hegelich, K. J. Bowers, K. A. Flippo, T. J. T. Kwan, and J. C. Fernandez, Phys. Plasmas 14, 056706 (2007).
[17] A. Henig, D. Kiefer, K. Markey, D. C. Gautier, K. A. Flippo, S. Letzring, R. P. Johnson, T. Shimada, L. Yin, B. J. Albright, K. J. Bowers, J. C. Fernandez, S. G. Rykovanov, H.-C. Wu, M. Zepf, D. Jung, V. Kh. Liechtenstein, J. Schreiber, D. Habs, B. M. Hegelich, Phys. Rev. Lett. 103, 045002 (2009).
[18] S. Palaniyappan, B. M. Hegelich, H. C. Wu, D. Jung, D. C. Gautier, L. Yin, B. J. Albright, R. P. Johnson, T. Shimada, S. Letzring, D. T. Offermann, J. Ren, C. Huang, R. Hörlein, B. Dromey, J. C. Fernandez, and R. C. Shah, Nat. Phys. 8, 763 (2012).
[19] S. Palaniyappan, C. Huang, D. C. Gautier, C. E. Hamilton, M. A. Santiago, C. Kreuzer, A.B. Sefkow, R. C. Shah, and J. C. Fernández, Nat. Commun. 6, 10170 (2015).
[20] J. Psikal, V. T. Tikhonchuk, J. Limpouch, A. A. Andreev, and A. V. Brantov, Phys. Plasmas 15, 53102 (2008).
[21] A. J. Mackinnon, Y. Sentoku, P. K. Patel, D. W. Price, S. Hatchett, M. H. Key, C. Andersen, R. Snavely, and R. R. Freeman, Phys. Rev. Lett. **88**, 2150061 (2002).
[22] S. Buffechoux, J. Psikal, M. Nakatsutsumi, L. Romagnani, A. Andreev, K. Zeil, M. Amin, P. Antici, T. Burris-Mog, A. Compant-La-Fontaine, E. D'Humières, S. Fourmaux, S. Gaillard, F. Gobet, F. Hannachi, S. Kraft, A. Mancic, C. Plaisir, G. Sarri, M. Tarisien, T. Toncian, U. Schramm, M. Tampo, P. Audebert, O. Willi, T. E. Cowan, H. Pépin, V. Tikhonchuk, M. Borghesi, and J. Fuchs, Phys. Rev. Lett. **105**, 015005 (2010).
[23] A. Henig, D. Kiefer, M. Geissler, S. G. Rykovanov, R. Ramis, R. Hörlein, J. Osterhoff, Z. Major, L. Veisz, S. Karsch, F. Krausz, D. Habs, and J. Schreiber, Phys. Rev. Lett. 102, 095002 (2009).
[24] T. D. Arber, K. Bennett, C. S. Brady, A. Lawrence-Douglas, M. G. Ramsay, N. J. Sircombe, P. Gillies, R. G. Evans, H. Schmitz, A. R. Bell, and C. P. Ridgers, Plasma Phys. Control. Fusion 57, 113001 (2015).
[25] A. P. L. Robinson, P. Gibbon, M. Zepf, S. Kar, R. G. Evans, and C. Bellei, Plasma Phys. Control. Fusion 51, 024004 (2009).
[26] B. Qiao, M. Zepf, P. Gibbon, M. Borghesi, B. Dromey, S. Kar, J. Schreiber, and M. Geissler, Phys. Plasmas 18, 43102 (2011).
[27] R. Thevamaran, E. R. Meshot, and C. Daraio, Carbon N. Y. 84, 390 (2015).
[28] G. M. Petrov and J. Davis, Phys. Plasmas 18, 073102 (2011).
[29] G. M. Petrov and J. Davis, Commun. Comput. Phys. 16, 599 (2014).
[30] G. M. Petrov, J. Davis and Tz. Petrova, Plasma Phys. Control. Fusion 51, 095005 (2009).